Acta Materialia 294 (2025) 121074

Contents lists available at ScienceDirect

Acta Materialia

journal homepage: www.elsevier.com/locate/actamat

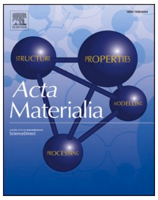

Thermodynamic analysis and modeling of Pd-Ni-S bulk metallic glass-forming system

Maryam Rahimi Chegeni [a,*], Wenhao Ma [b], Sascha Sebastian Riegler [a], Amirhossein Ghavimi [a], Magnus Rohde [b], Fan Yang [c], Hans Jürgen Seifert [b], Isabella Gallino [d], Ralf Busch [a]

[a] Saarland University, Chair of Metallic Materials, Campus C6.3, 66123 Saarbrücken, Germany
[b] Karlsruhe Institute of Technology, Institute for Applied Materials - Applied Materials Physics (IAM-AWP), Hermann-von-Helmholtz-Platz 1, 76344 Eggenstein-Leopoldshafen, Germany
[c] Institut für Materialphysik im Weltraum, Deutsches Zentrum für Luft- und Raumfahrt (DLR), 51170 Köln, Germany
[d] Technical Univerisity of Berlin, Chair of Metallic Materials, Ernst-Reuter-Platz 1, 10587 Berlin, Germany

ARTICLE INFO

Keywords:
Calphad modeling
Metallic glasses
Nucleation and growth
Fast differential scanning calorimetry
TTT diagram

ABSTRACT

This study explores both experimental and computational aspects of the thermophysical properties of the novel ternary BMG-forming Pd-Ni-S system. Unlike more complex quinary BMG-formers, this ternary system's simplicity allows for applying the CALPHAD approach to model the underlying thermodynamics governing glass formation.

Experimental investigations include quantifying specific heat capacity and studying crystallization across various compositions critical for generating essential input data. Using a two-state approach, initial modeling of the undercooled liquid and glass is conducted for individual elements and extended to the ternary system. Model predictions are validated against experimental findings and iteratively optimized. Using the parallel tangent method, the Gibbs free energy of crystalline and liquid phases at different compositions are calculated, providing a more accurate estimation of the nucleation driving force of the first forming phase compared to the conventional thermodynamic approach. These calculated driving forces are then used to model the isothermal Time-Temperature-Transformation (TTT) diagrams, and finally for the estimation of the interfacial energy between liquid and crystal during primary crystallization, which plays an important role in the glass-forming ability of this system. The experimental and calculated results are found to be compatible for near-eutectic compositions.

1. Introduction

Metallic glasses are disordered and thermodynamically unstable materials formed by rapid cooling of highly viscous melts, which slows down crystallization and preserves the amorphous structure. Following the discovery of the first Au-Si amorphous metal by Duwez et al. [1], researchers have developed bulk metallic glasses (BMGs) with high glass-forming ability (GFA) by increasing the amount of alloying elements and optimizing compositions. This effort has led to various BMG-forming systems based on elements such as copper (Cu) [2], iron (Fe) [3], nickel (Ni) [4], palladium (Pd) [5], titanium (Ti) [6], and zirconium (Zr) [7]. However, identifying optimal glass-forming compositions experimentally is time-consuming and challenging due to the vast number of possible combinations. Therefore, there is a need for computational methods to describe the thermodynamics of metallic glasses and identify the maxima in alloy glass forming ability (GFA).

The CALPHAD (CALculation of PHAse Diagrams) method is a powerful computational technique used to predict the thermodynamic properties of different systems. This approach integrates experimental data and theoretical models to generate phase diagrams, which are crucial for understanding the phase transitions within the materials across different compositions and temperatures. Originating at the end of the 1960s and in the early 1970s, CALPHAD has evolved into an essential tool in materials science, aiding in the design and development of new materials with tailored properties [8].

The CALPHAD methodology is a great tool for use in the field of BMGs, thanks to the continuous advancements in thermodynamic modeling and calculation techniques to describe the Gibbs free energy of

---

* Corresponding author.
E-mail address: maryam.rahimi_chegeni@uni-saarland.de (M. Rahimi Chegeni).

https://doi.org/10.1016/j.actamat.2025.121074
Received 28 September 2024; Received in revised form 9 April 2025; Accepted 21 April 2025

both crystalline and non-crystalline phases [9]. However, attaining precise modeling for amorphous alloys using the CALPHAD method has proven somewhat elusive due to several factors, despite varying levels of success in different attempts [10–12]. This modeling is intrinsically difficult because of the disordered structure and the need to describe the glass transition and short-range order (SRO) as well as medium-range order (MRO). The second-generation CALPHAD database, proposed by SGTE (Scientific Group Thermodata Europe), lacks proper modeling of the (undercooled) liquid down to the glass transition temperature. Its polynomial description restricts the extrapolation of the Gibbs free energy expression to the metastable region, where less thermodynamic data is available. In contrast, the third-generation CALPHAD database [13] and the two-state liquid model, which describes the liquid as a mixture of two distinct states and provides a more realistic representation of the thermodynamic properties [14], offer a more physically sound description, enhancing reliability in property extrapolation. Nevertheless, a concrete model and methodology are still missing for bulk metallic glass-forming systems, characterized by complex interatomic behaviors such as pronounced SRO and MRO in the metastable undercooled liquid phase.

In this study, the third-generation CALPHAD approach is implemented and expanded for a more physically sound and reliable modeling of the undercooled liquid. The focus is on the newly developed ternary bulk metallic glass forming alloy system, Pd-Ni-S [15]. In terms of equilibrium thermodynamics, this system was for the first time extensively studied by Karup-Moller et al. [16] in 1993. They produced and annealed numerous samples of different compositions in the ternary system at temperatures of 1173 K, 998 K, 823 K, and 673 K, for extended periods, and quenched them subsequently to analyze the available phases. The result of their work provides comprehensive first-hand data on the equilibrium thermodynamics of this system, serving as crucial input for CALPHAD modeling.

More recently, the system was studied by Kuball et al. in terms of glass-forming ability [15]. Fig. 1 shows the shaded area identified by Kuball et al. as the glass-forming region. In his work, Kuball introduced $Pd_{31}Ni_{42}S_{27}$ composition as a good glass former with a critical casting thickness of 1.5 mm and good thermal stability, as well as $Pd_{37}Ni_{37}S_{26}$ composition, which has less thermal stability but is likely closest to the eutectic due to its short melting interval [15]. As shown in Fig. 1, the glass-forming region is surrounded by the equilibrium phases of Ni_3S_2, (Pd, Ni) solid solution, and Pd_4S in its stable crystalline state, indicating the simplicity of the system's equilibrium thermodynamics. This makes it an excellent candidate for thermodynamic modeling using CALPHAD due to its uncomplicated characteristics.

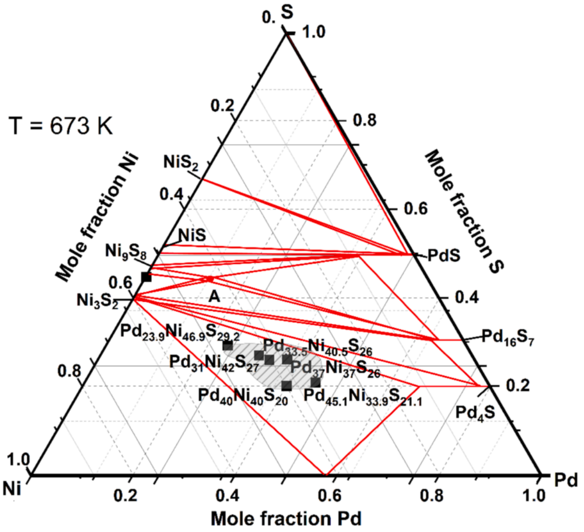

Fig. 1. Position of investigated Pd-Ni-S compositions in the ternary phase diagram (black squares), located within the shaded glass-forming region (GFR), determined by Kuball et al. [15]. The isothermal ternary phase diagram is taken from ref [16].

Our experimental investigations include both binary and ternary compositions within this ternary system. The ternary compositions are chosen from the glass-forming region depicted in Fig. 1 to further develop input data for CALPHAD calculations.

In our work, a new thermodynamic dataset for the Pd-Ni-S ternary system is established to describe the thermodynamics of stable phase diagrams (binary and ternary) and the metastable equilibrium state of the undercooled liquid. The available experimental data on the equilibrium phase diagram from the literature, as reported in the works of Karup-Moller et al. [16] are assessed and used as input data for CALPHAD modeling. In our experimental work, different glass forming alloy compositions, namely $Pd_{23.9}Ni_{46.9}S_{29.2}$, $Pd_{33.5}Ni_{40.5}S_{26}$, $Pd_{37}Ni_{37}S_{26}$, $Pd_{40}Ni_{40}S_{20}$, and $Pd_{45.1}Ni_{33.9}S_{21.1}$ are produced and studied using a range of techniques, including calorimetry, where we employ methods such as Differential Scanning Calorimetry (DSC), Differential Thermal Analysis (DTA), and Flash-DSC (chip-calorimetry). The glass transition, crystallization, and liquidus temperatures; the enthalpies of crystallization and fusion, as well as the isobaric specific heat capacity of glassy, crystalline, and liquid state are determined, which serve as important input data for CALPHAD modeling and are further used to calculate the thermodynamic functions of excess enthalpy, entropy, and Gibbs free energy between liquid and the crystalline mixture. To further strengthen our CALPHAD model, the published thermodynamic data for $Pd_{31}Ni_{42}S_{27}$ from the work of Kuball et al. [15,17] are incorporated in the model. The data are especially useful because they include specific heat capacity measurements in the supercooled liquid region, which were obtained for this more thermally stable composition and are essential for accurate modeling of the (undercooled) liquid. Subsequently, using CALPHAD, the driving force for crystallization at different compositions is calculated by applying the parallel tangent method to the Gibbs free energy of the crystalline and liquid phases [18], which provides a more accurate estimation of the driving force for nucleation of the first forming phase than the excess Gibbs free energy estimations based only on the thermodynamic measurements. The calculated driving forces are then used to model the isothermal Time-Temperature-Transformation (TTT) diagrams, which yield the interfacial energy between the liquid and crystal during primary crystallization, crucial for understanding the glass-forming ability of this system. Moreover, the study incorporates microstructural analyses using high-energy synchrotron diffraction experiments (HEXRD), which are compared with CALPHAD calculations to enhance the accuracy of the modeling based on the phase formation results.

2. Experimental methods

2.1. Sample synthesis

Fig. 1 shows the selected compositions of the Pd-Ni-S system that were studied in a ternary isothermal section of the phase diagram at *673* K. The Pd-Ni-S pre-alloys were prepared by inductively melting the high-purity raw elements Pd (99.999 wt %), Ni (99.995 wt %), and S (99.9995 wt %) in silica quartz tubes under a high-purity argon atmosphere (99.9999 wt %). Subsequently, the pre-alloys were fluxed by remelting them in dehydrated B_2O_3 to reduce the number of heterogeneous nucleation sites, as described in [19] and finally were melted in an arc furnace together with the missing amounts of elements to reach the selected compositions. The master alloys of binary and ternary compositions with marginal GFA were inductively re-melted, and subsequently melt spun onto a rotating copper wheel to obtain thin ribbons of approximately 20–50 μm thickness. The melt spinning parameters were adjusted according to each alloy system's melting point and viscosity and the amorphous state of every sample was evaluated via X-ray diffraction with a PANalytical X'Pert Pro diffractometer.

2.2. DSC and DTA experiments

Thermal analysis was carried out using a power-compensated Perkin Elmer DSC 8000 under a constant flow of 20 ml min^{-1} high-purity Argon atmosphere (99.9999 wt %). For low temperature measurements up to a maximum temperature of 723 K, Al-pans were used. For examinations in higher temperature regions up to a maximum temperature of 973 K graphite crucibles were utilized. For low-temperature measurements, each sample was remeasured after crystallization, using the signal of the resulting crystalline mixture as a baseline. To study the melting events up to very high temperatures, a NETZSCH STA 449 Jupiter differential thermal analyzer (DTA) was used.

The absolute value of the specific heat capacity in the glassy, crystalline, and supercooled liquid state was determined in a power-compensated Perkin Elmer DSC8500 equipped with a three-stage intracooler. Measurements were performed in aluminum pans upon heating in reference to the specific heat capacity of a sapphire standard using a step method described in detail in [20,21]. To determine the specific heat capacity in the liquid state the same method was applied to the same samples from the low-temperature measurements in the DSC using graphite crucibles.

2.3. Fast differential scanning calorimetry (FDSC) experiments

Fast Differential Scanning Calorimetry (FDSC) measurements were performed via Mettler-Toledo FDSC2+ using a MultiSTAR UFH 1 high-temperature chip sensor with silicon nitride (Si_3N_4) surface based on MEMS-sensor technology, allowing for heating up to 1273 K [22]. The attached Huber HC100 intracooler allows cooling rates of up to 40,000 K/s, keeping the sensor support temperature at 188 K, which ensures accurate and reliable measurements. During the whole measuring process, the system was continuously purged using a high-purity (99.9999 wt %) argon gas flow of 60 ml/min to prevent oxidation of the metallic samples. Samples were cut from the melt-spun ribbons under a stereomicroscope using a micro-scalpel and were transferred to the active sensor area with the help of a fine hair with a thickness of approximately 50 to 100 $^{\mu m}$ (μm). The samples were melted afterward via several moderate heating scans (50 K/s) to temperatures above liquidus temperature to ensure an intimate thermal contact between the sample and sensor. The sample mass was optimized to prevent sample size effects on thermal stability, such as the dependence of critical cooling and heating rates on sample mass [23,24], by calculating the ratio of the measured enthalpy of fusion in FDSC to the enthalpy of fusion determined in a conventional DSC8000 [24,25]. The eutectic temperature determined in the conventional DSC was used to correct the temperature offset of the FDSC sensors [26].

Using FDSC, critical cooling rate (CCR) experiments were conducted to determine the minimum required cooling rate (R_c) needed to bypass crystallization. These experiments were carried out only for three better glass-forming compositions, namely $Pd_{31}Ni_{42}S_{27}$\$E, $Pd_{33.5}Ni_{40.5}S_{26}$, and $Pd_{37}Ni_{37}S_{26}$. The methodology described in [25] was followed, applying various cooling rates ranging from 1 to 40,000 K/s.The rest of the compositions could not reach the glassy state even with the very high cooling rates applicable by FDSC.

Isothermal crystallization studies via Time-Temperature-Transformation (TTT) diagrams were also carried out in FDSC for the same alloys. The thermal protocol of the samples consisted of heating above the liquidus temperature at 773, 823, and 973 K with a holding time of 1 and 10 s to see the effect of different parameters on the final TTT diagram, followed by quenching at a rate of 40,000 K s^{-1} to the desired isothermal temperature.

The assessment of atomic mobility in the terms of relaxation time was also carried out using FDSC via the Step response analysis method during cooling with a base frequency of 10 Hz [27]. Samples were cooled with 40,000 K/s to bypass the crystallization and further temperature down jumps of 2 K with a cooling rate of 2000 K/s followed by isothermal holding of 0.1024 s were applied. These temperature down-jumps of 2 K are small enough to ensure the linearity of the response, since the thermal fluctuations of the glass-forming systems are known to be larger than 2 K [28,29], enabling us to assess the atomic dynamics associated with the glass transition, most importantly α-relaxation [27,28,30]. A detailed description of this methodology can be found in [31].

2.4. High-energy synchrotron X-ray diffraction

The formation of the primary phase in the alloys upon undercooling was studied using in-situ wide-angle X-ray scattering (WAXS) experiments carried out at the Deutsches Elektronen- Synchrotron (DESY) in Hamburg, Germany. Samples with various compositions were heated to a fully molten state and then cooled down with an average cooling rate of about 200 K/s. All experiments were carried out under aerodynamic levitation condition (ADL) to minimize the impact of heterogeneous nucleation [32]. This method is better suited to Pd-Ni-S compositions in comparison to electrostatic levitation, due to their high vapor pressure. The samples were investigated in transmission mode at the high-intensity beamline facility P21.1 at PETRA III. A wavelength of 0.12215 Å was employed. Using an acquisition time of 0.3 s per frame, the intensity data were collected with a Perkin Elmer XRD1621 CsI bonded amorphous silicon detector, featuring a resolution of 2048 × 2048 pixels. The two-dimensional X-ray diffraction patterns of the samples were subsequently integrated to obtain the intensity I(Q) using the software package PyFAI (Python Fast Azimuthal Integration) [33]. Finally, the obtained data were compared with the simulated diffraction data of the equilibrium phases using the Vesta software [34].

2.5. CALPHAD modeling

Pure sulfur and palladium are modeled within the third-generation CALPHAD database approach. The description of pure Nickel is taken from the previous assessment of Hao et al. [35]. The available published data on thermodynamic and thermophysical properties of the Ni-S, Pd-S, and Ni-Pd binary systems are comprehensively assessed and used for the Gibbs free energy description of the solid phases.

The evaluation and optimization of the Pd-Ni-S ternary system dataset is carried out based on the experimental study of Karup-Moller and Makovicky, as it provides comprehensive equilibrium phase diagram data at the isothermal temperatures of 673 K, 823 K, 998 K, and 1173 K [16].

The third-generation database approach employs the two-state liquid model to describe the “liquid-amorphous phase “in a unary system [36]. This approach allows a more reliable extrapolation of the Gibbs free energy to the temperature ranges where experimental data are difficult to obtain, which is suitable for the assessment of the undercooled liquid.

In this work, we extend this methodology for the glass-forming Pd-Ni-S ternary system to better describe the undercooled liquid, where complex interatomic interactions significantly influence its properties and the glass-forming mechanism. The description of the liquid phase applies the two-state liquid model within the framework of the third-generation database approach. The short-range order of the ternary liquid phase [37] is described by the ionic two-sublattice model [38]: $(Ni^{2+},Pd^{2+})_P(S^{2-}, Va)_Q$, where P and Q are the number of sites on the two sublattices, which are varied with composition to ensure electroneutrality, and Va is the hypothetical vacancies introduced into the anion sublattice.

The specific heat capacity of the glassy state is assumed to be similar to the corresponding mixture of the crystalline phases, which is approximated using the Kopp-Neumann rule [39]. This assumption is valid, as demonstrated by the previous analysis conducted by Kuball et al. [17], which shows that for the $Pd_{31}Ni_{42}S_{27}$ glass-forming alloy, as well as in our own research (Fig. 3) and other studies [40,41], the specific heat capacity (c_p) of the glass matches that of the crystal up to temperatures just below the glass transition region.

Lack of data for the undercooled liquid is another challenge for this analysis, as the behavior of the undercooled liquid cannot be easily predicted. For this reason in this work, we incorporate experimental data across various compositions to serve as input for fitting the heat capacity, enthalpy of formation, and enthalpy of fusion. Additionally, the acquired cp data within the supercooled liquid region of $Pd_{31}Ni_{42}S_{27}$ [17], known for being the more thermally stable composition, are also used to improve the model. This promises a self-consistent dataset that can adequately describe the thermodynamic behaviors of the Pd-Ni-S system in the glass-forming range.

This modeling approach also needs to meet the following criteria: (1) the thermodynamic properties should be continuous at different segments; and (2) The calculated isentropic temperature must be lower than the experimentally determined T_g. A detailed description of the modeling of the Pd-Ni-S ternary system will be provided in a forthcoming publication.

3. Results

3.1. Thermodynamic studies

3.1.1. Experimental thermal and thermodynamic data

In the first step, the important thermal and thermodynamic data of the different Pd-Ni-S alloys were investigated. This includes the determination of the glass transition temperature (T_g); crystallization temperature (T_x); enthalpy of crystallization (ΔH_x); eutectic temperature (T_{eu}); liquidus temperature (T_l) and enthalpy of fusion (ΔH_m) upon standard scan and also specific heat capacity functions c_p (T) of the crystalline mixture, glasses, undercooled liquids and melts. These properties are important in terms of further thermodynamic and kinetic analysis and serve as important input data for CALPHAD modeling. In particular, experimental heat capacity data of the melt and undercooled liquid are used for the proper modeling of the liquid phase in the CALPHAD approach and the enthalpies of crystallization and fusion serve as input data for this modeling of the liquid.

Fig. 2 (a-b) shows the up scans acquired for different compositions during heating with 20 K/min through DSC and DTA (blue and red curves, respectively). The onset temperatures of the glass transition, T_g, crystallization, T_x, eutectic $T_{eu,}$ and liquidus temperatures T_l were determined using a tangent construction. The crystallization enthalpy, ΔH_x, and the heat of fusion, ΔH_m, were determined by integrating the area between the curve and the baseline. All the evaluated data are listed in Table 1. It is interesting to note that entropies of fusion for these alloys are quite high compared to Richard's rule for metals (≈ 2.2 cal K^{-1} mol^{-1}), and also higher than the entropies of fusion in most other bulk metallic glass forming alloys [42] which is likely due to covalent contributions of the sulfur acting as a metalloid with the metallic species. The heat flow profile of Pd-Ni-S variations in Fig. 2(a) displays a weak endothermic jump that corresponds to the glass transition due to the difference in heat capacity of glass and supercooled liquid. Additionally, these alloys exhibit exothermic events associated with the crystallization process. Regarding other compositions, $Pd_{37}Ni_{37}S_{26}$ predominantly crystallizes via a single distinct peak, suggesting its proximity to the actual eutectic point within this ternary system. Already Kuball et al. [15], in their alloy development framework, demonstrated that this alloy exhibits the narrowest melting interval ($T_l - T_m$) in regard to many other developed compositions, signifying its proximity to the eutectic point. These compositions also exhibit a notably limited supercooled liquid region ($T_x - T_g$) as can be seen in Fig. 2(a) and from the determined ΔT ($T_x - T_g$) values presented in Table 1, indicating their poor thermal stability. Consequently, further measurements within the supercooled liquid, such as c_p (heat capacity) measurements and relaxation studies, become problematic. With changing Pd content towards alloys with larger Pd content, the enthalpy and entropy of fusion decreases slightly.

Focusing on Fig. 2(b), changes in the eutectic and liquidus temperature and the shape of the melting peaks can be monitored as well. In the case of $Pd_{40}Ni_{40}S_{20}$ and $Pd_{45.1}Ni_{33.9}S_{21.1}$, determining the liquidus temperature from the main apparent melting peak is misleading and as observed in synchrotron measurements during heating, the (Pd, Ni) solid solution is stable up to very high temperatures and the liquidus temperature could be only roughly estimated based on the measured HEXRD patterns and the temperatures associated with them (see supplementary material, SI Figure 1). Also during cooling experiments, (Pd, Ni) solid solution tends to form as the first phase around the same temperature region.

As expected and as can be seen in Fig. 2(b), the determined eutectic temperatures of all the Pd-Ni-S alloy variations are in the same range, specifying a eutectic temperature of 724 ± 3 K. In respect to the shape of the melting peaks, $Pd_{23.9}Ni_{46.9}S_{29.2}$, $Pd_{45.1}Ni_{33.9}S_{21.1,}$ and $Pd_{40}Ni_{40}S_{20}$ show a shoulder respectively on their right and left side, indicating their off-eutectic behavior, while $Pd_{33.5}Ni_{40.5}S_{26}$ and $Pd_{37}Ni_{37}S_{26}$ are melting through one single peak, showing their proximity to the eutectic point as

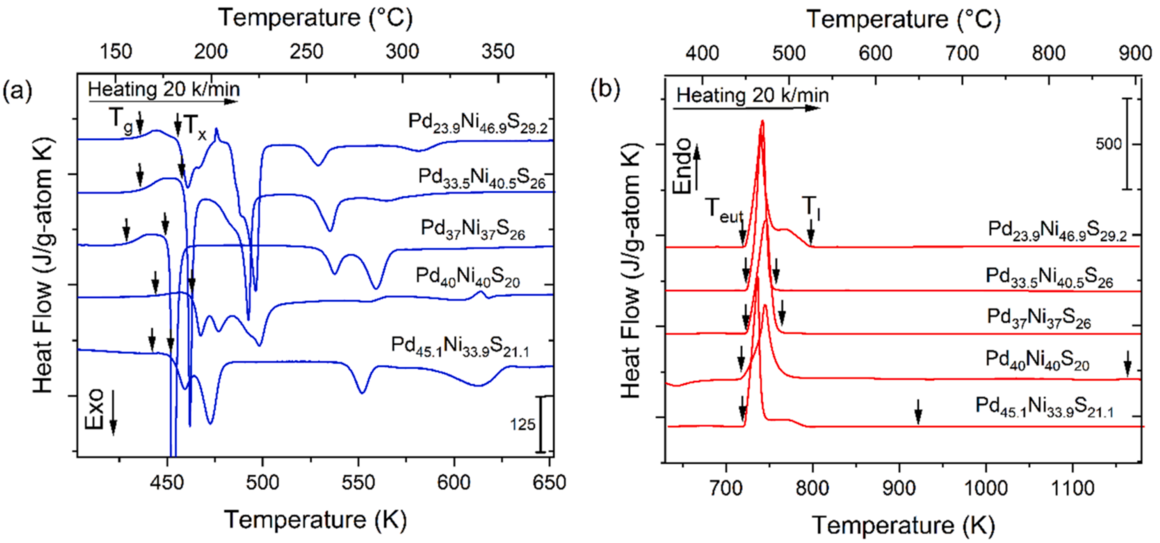

Fig. 2. Heat flow curves resulted from, a-b) DSC (blue curve) and DTA (red curve) scans of Pd-Ni-S variations acquired during heating with 20 K/min, the glass transition temperature (T_g), crystallization temperatures (T_x), eutectic temperatures (T_{eu}) and liquidus temperatures (T_l) are indicated with black arrows.

Table 1

Measured characteristic temperatures and enthalpies for Pd-Ni-S variations: glass transition temperature (T_g), crystallization onset temperature (T_x), eutectic temperature (T_{eu}) and liquidus temperature (T_l), enthalpy of crystallization (ΔH_x), enthalpy of fusion (ΔH_m), and entropy of fusion ($\Delta S_m = \Delta H_m / T_l$). Measurements are conducted with a heating rate of 20K/min.

Composition	T_g (K)	T_x (K)	ΔT (T_x-T_g) (K)	ΔH_x (kJ/g-atom)	T_{eu} (K)	T_l (K)	ΔH_m (kJ/g-atom)	ΔS_m ($\Delta H_m/T_l$) (J/g-atom K)
$Pd_{23.9}Ni_{46.9}S_{29.2}$	434	456	22	−5.428	723	791	12.076±0.203	15.26
$Pd_{33.5}Ni_{40.5}S_{26}$	434	459	25	−5.553	729	750	11.025-±0.147	14.7
$Pd_{37}Ni_{37}S_{26}$	426	451	25	−4.894	726	757	10.726±0.162	14.17
$Pd_{40}Ni_{40}S_{20}$	441	462	21	−3.867	721	1173	10.131±0.450	8.64
$Pd_{45.1}Ni_{33.9}S_{21.1}$	438	452	14	−4.616	721	923	10.392±0.339	11.26

discussed earlier.

3.1.2. Isobaric specific heat capacity

The measured specific heat capacities for the glassy, crystalline, and liquid states using the step method [20,43] are exemplarily shown for $Pd_{37}Ni_{37}S_{26}$ in Fig. 3. The complete data for all the compositions can be found in the supplementary material. Heat capacity data on the alloy $Pd_{31}Ni_{42}S_{27}$ was previously published in Ref. [17] and is used in further analysis. The model of Inaba [44] can be used to represent the variation of heat capacity with temperature of glassy and crystalline mixture around the Debye temperature (T_D) as

$$c_p^{g/x} = 3R \Big/ M\{1 - \exp(-1.5T / T_D)\}, \tag{1}$$

in which M and T_D are fitting parameters, R is the universal gas constant and T is the absolute temperature. At temperatures far above the T_D, the temperature dependencies of liquid and crystal specific heat capacity, $c_p^l(T)$ and $c_p^x(T)$, are fitted using the Kubaschewski equations [45]

$$c_p^l = 3R + aT + bT^{-2} \tag{2}$$

and

$$c_p^x = 3R + cT + dT^2, \tag{3}$$

where R is the universal gas constant and a, b, c, and d are acquired fitting parameters listed in Table 2. To evaluate the accuracy of the obtained specific heat capacity functions, the area between the specific heat capacity curves of the liquid and crystalline phase is estimated for the interval between the onset temperature of crystallization (T_x) and liquidus temperature (T_l). This value should be equal to the difference between the enthalpy of fusion and the enthalpy of crystallization, which is described as

$$\Delta H_m - \Delta H_x = \int_{T_x}^{T_l} \Delta c_p^{l-x} dT. \tag{4}$$

As shown in Fig. 3 for $Pd_{37}Ni_{37}S_{26}$, the integral of the shaded area yields a value of 5.7 kJ g-atom^{-1} and $\Delta H_m - \Delta H_x$ equals to 5.8 kJ g-atom^{-1}, representing a difference of <2 %, which validates the reliability of the c_p measurements.

At temperatures lower than the glass transition but above the Debye temperature, both the glassy and crystalline alloy exhibit similar specific heat capacities, reaching a c_p of about 3 R (≈25 J g-atom $^{-1}$ K $^{-1}$) at ambient temperature which is in line with the rule of Dulong-Petit [20, 41,46,47]. At approximately 350 K, the c_p of the glass starts to deviate from that of the crystal because of relaxation effects and finally after the glass transition range, it is expected to reach the c_p of the supercooled liquid. However, due to the poor thermal stability of the supercooled liquid and the interference of crystallization, no c_p data in the supercooled liquid could be collected.

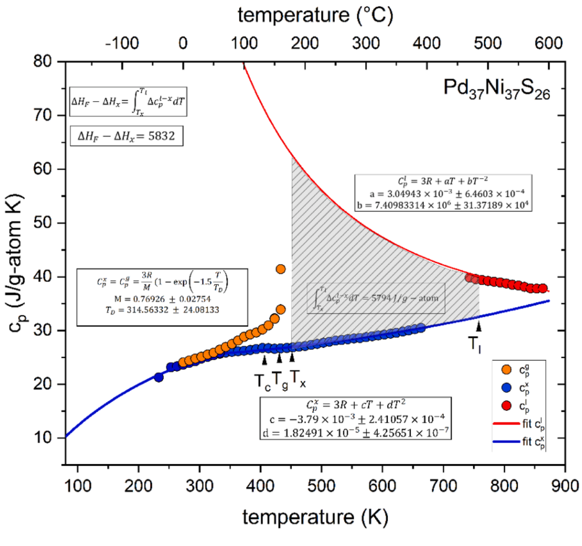

Fig. 3. Isobaric specific heat capacity data of glassy c_p (orange circles), liquid (red circles), and crystalline state (blue circles) for $Pd_{37}Ni_{37}S_{26}$. The fits of crystalline (blue full line) and liquid states (red full line) are based on the Inaba and Kubaschewski equations, Eq. (1), (2), and (3).

3.1.3. Excess enthalpy, entropy and Gibbs free energy

From the measured specific heat capacity data and the DSC scan data for the liquidus temperature T_l, heat of fusion, ΔH_m, and entropy of fusion, ΔS_m, the enthalpy and entropy difference between the (undercooled) liquid and the crystalline mixture $\Delta H^{l-x}(T)$, $\Delta S^{l-x}(T)$ can be calculated as [21]

$$\mathbf{\Delta H^{l-x}(T) = \Delta H_m + \int_{T_l}^{T} \Delta c_p^{l-x}(T')dT'}, \tag{5}$$

and

$$\mathbf{\Delta S^{l-x}(T) = \Delta S_m + \int_{T_l}^{T} \frac{\Delta c_p^{l-x}(T')}{T'} dT'}. \tag{6}$$

Finally, the Gibbs free energy difference between the undercooled liquid and the crystalline mixture is calculated as a function of temperature using the following equation

$$\Delta G^{l-x}(T) = \Delta H^{l-x}(T) - T \times \Delta S^{l-x}(T). \tag{7}$$

In the real nucleation process a driving force exists as soon as the melt is cooled below the T_l. This driving force is the chemical potential difference between the liquid and crystalline nucleus. In our simplistic approach, the Gibbs free energy difference between the supercooled liquid and the crystalline mixture is assumed to be equal to the chemical potential.. In the case of very off-eutectic systems, like $Pd_{40}Ni_{40}S_{20}$ and $Pd_{45.1}Ni_{33.9}S_{21.1}$ which show a high-temperature shoulder during melting, it may lead to underestimations of the excess enthalpy, entropy, and Gibbs free energy. However, it is reasonable to consider the liquidus temperature T_l as a reference point where $\mathbf{\Delta G^{l-x}}$ is considered to be zero,

Table 2

Fitting parameters derived from applying Eq. (1), (2), and (3) to the specific heat capacity data.

Fitting Parameter / alloy	$Pd_{23.9}Ni_{46.9}S_{29.2}$	$Pd_{33.5}Ni_{40.5}S_{26}$	$Pd_{37}Ni_{37}S_{26}$	$Pd_{40}Ni_{40}S_{20}$	$Pd_{45.1}Ni_{33.9}S_{21.1}$
$\mathbf{a}.\ 10^3\ (\mathbf{J\ g-atom^{-1}K^{-2}})$	2.71 ± 0.2973	4.61 ± 0.2355	3.0494 ± 0.6460	$10.79\ \times\ \pm 0.1665$	8.54 ± 0.3163
$\mathbf{b}.\ 10^{-6}\ (\mathbf{J\ K\ g-atom^{-1}})$	7.1332 ± 0.1715	7.6974 ± 1.2577	7.4098 ± 0.3137	3.8876 ± 0.0769	4.2788 ± 0.1524
$\mathbf{c}.\ 10^3\ (\mathbf{J\ g-atom^{-1}K^{-2}})$	-10.45 ± 0.2284	0.4169 ± 0.2026	-3.79 ± 0.2410	-2.7 ± 0.1529	-11.59 ± 0.5716
$\mathbf{d}.\ 10^6\ (\mathbf{J\ g-atom^{-1}K^{-3}})$	23.8208 ± 0.4033	13.5481 ± 0.3578	18.2491 ± 0.4256	13.7149 ± 0.2709	24.6858 ± 0.9985
$\mathbf{M}.\ 10^2$	91.29 ± 0.607	$85.706\ \pm\ 0.646$	$76.926\ \pm\ 2.754$	$83.50\ \pm\ 1.12$	$99.681\ \pm\ 0.574$
$\mathbf{T_D}(\mathrm{K})$	256.7726 ± 4.5464	$201.2505\ \pm\ 5.3148$	$314.5633\ \pm\ 24.0813$	$243.4713\ \pm\ 9.3483$	$185.7713\ \pm\ 4.1716$

as there is a driving force for crystallization in multi-component systems just below this temperature.

The calculated thermodynamic excess functions for $Pd_{37}Ni_{37}S_{26}$ determined from the experimental data using Eqs. (5-7) are plotted in Fig. 4. The data for the other compositions can be found in supplementary materials. The $\mathbf{\Delta H^{l-x}(T)}$ function shows a decrease with decreasing temperature, bearing a smaller value than $\mathbf{\Delta H_m}$, because of the continuous increase in the heat capacity difference of the undercooled liquid and crystalline phases (Fig. 3). This function illustrates the changes in the crystallization enthalpy as depicted in Fig. 4. The circles show independently measured crystallization enthalpies during isothermal holding at the respective temperature through FDSC measurements for $Pd_{37}Ni_{37}S_{26}$. These measured enthalpy differences are in good agreement with the $\mathbf{\Delta H^{l-x}(T)}$ function calculated through Eq. (5), confirming the consistency with the experimentally measured c_p as a function of temperature.

Fig. 4 also shows the temperature scaled entropy difference between the crystalline mixture and the undercooled liquid. The high value of the enthalpy of fusion (10.7 kJ g-atom^{-1}) in combination with the low liquidus temperature of the alloy results in a high entropy of fusion (14.17 J g-atom^{-1} K), which leads to a dramatic drop of the entropy in the supercooled liquid region and yields the negative slope of $\mathbf{\Delta G^{l-x}}$. Based on the assumption of excess entropy being entirely configurational confirmed in [48,49], from the changes in $\mathbf{\Delta S^{l-x}}$, the Kauzmann temperature can be determined, below which the entropy of the amorphous solid would be lower than that of the crystal [50], lying only 20 degrees below T_g in this case.

3.1.4. CALPHAD modeling

The calculated isothermal sections of the Pd-Ni-S ternary phase diagram at 673 K, 823 K, and 998 K are presented in Fig. 5 (a-c), which agree well with the experimental results obtained by Karup-Moller and Makovicky (dashed blue lines) [16].

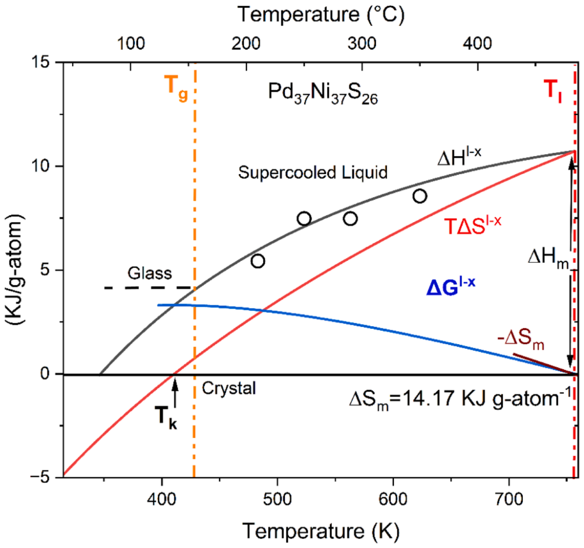

Fig. 4. Changes in excess enthalpy ΔH^{l-x}, entropy $\Delta S^{l-x}$and Gibbs free energy ΔG^{l-x} with undercooling for $Pd_{37}Ni_{37}S_{26}$ calculated using Eq. (5–7). Circles are ΔH_x values obtained during isothermal FDSC measurements.

The description of the liquid phase applies the two-state liquid model within the framework of the third-generation database approach. The short-range order of the ternary liquid phase is described by the ionic liquid model [38]: $(Ni^{2+},Pd^{2+})_P(S^{2-}, Va)_Q$. The ternary interaction parameter of the liquid phase incorporates an additional excess Gibbs free energy $-0.5bT^{-1}$ term, which is integrated from the Kubaschewski equation (Eq. (2) in Section 3.1.2), to adequately represent the thermodynamic behavior of the undercooled liquid.

However, the increase of the heat capacity by the decrease in temperature would lead to an unrealistic stabilization of the undercooled liquid at lower temperatures. Such behavior is prevented by introducing another segment at the experimental determined glass transition temperature, which lies around 435 K (±10 K) at various compositions. The low-temperature segment thus describes the thermodynamic properties of the glassy state. As indicated and shown previously, the heat capacities of the glass in the BMG forming Pd-Ni-S alloys are very close to their corresponding crystalline phases up to temperatures below their glass transition region. The heat capacities of the glassy state described by the Kopp-Neumann rule also matches very well with the experimental data, and are thus used for the Gibbs free energy description of the glassy state. This guarantees a self-consistent model which covers all the compositions in the glass-forming range.

The calculated heat capacities of the liquid phase at various compositions also agree well with the experimental data (Fig. 5d). Additionally, the calculated enthalpy change is also close to the results listed in Table 1. It can be concluded that the new thermodynamic dataset for the Pd-Ni-S ternary system can adequately describe the thermodynamic properties of the system. The thermodynamic assessment and the dataset will be published elsewhere.

3.2. Kinetic studies

3.2.1. Critical cooling rate determination

The findings from CCR measurements with an annealing temperature of 923 K and a holding time of 0.1 s are depicted in Fig. 6, illustrating the change in crystallization enthalpy in regards to the logarithmic scale of the applied cooling rate. In this study, due to the volatile nature of sulfur, samples couldn't be held at very high temperatures for a long time, otherwise, the composition would have changed and the sample could no longer be used. However, to avoid crystallization, it is crucial to subject the material to a degree of overheating and holding time well above the liquidus temperature [51,52]. This process dissolves heterogeneities or atomic clusters remaining from crystals [53–55]. These nuclei, if not dissolved, act as heterogeneous nucleation sites, negatively impacting the glass-forming ability (GFA) of the liquid, demanding a higher critical cooling rate, and finally affecting the shape of the Time-Temperature-Transformation (TTT) diagram [52]. Other possibilities like liquid to liquid transition (LLT) below or above T_l by the formation of ordered atomic clusters in metallic melts [56–58] or liquid to liquid separation (LLS) at temperatures above T_l [59,60] could also affect the homogeneity of melt. In [55], Q. Cheng et.al proved experimentally via fast scanning calorimetry that the homogenization

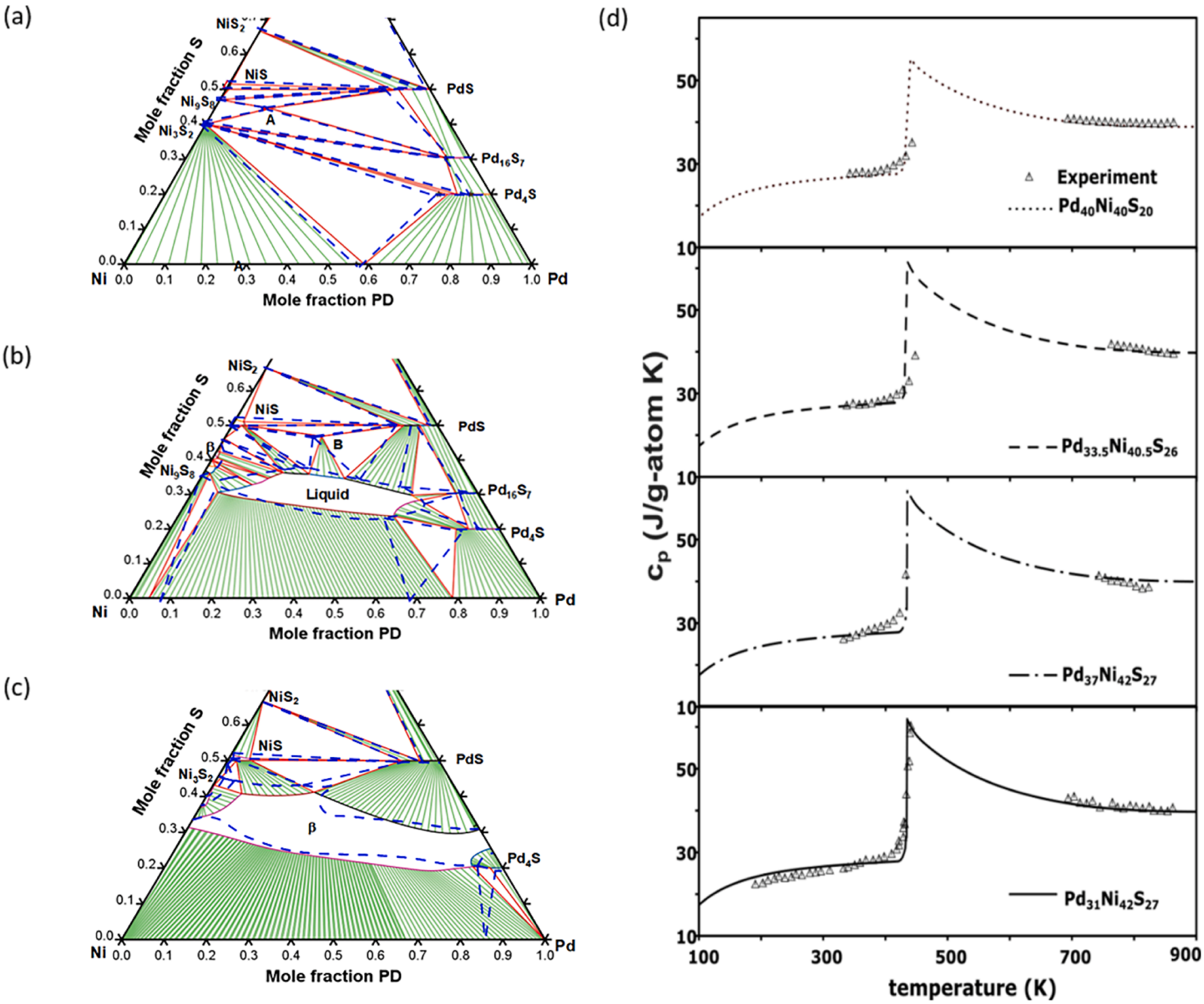

Fig. 5. Calculated isothermal sections of the Pd-Ni-S ternary phase diagram at (a) 673 K, (b) 823 K, and (c) 998 K, dashed blue lines indicate the experimental results obtained by Karup-Moller and Makovicky, (d) comparison between the calculated heat capacity and our experimental results for the indicated Pd-Ni-S glass forming compositions with the exception of c_p data of $Pd_{31}Ni_{42}S_{27}$, which were measured by kuball et.al [17].

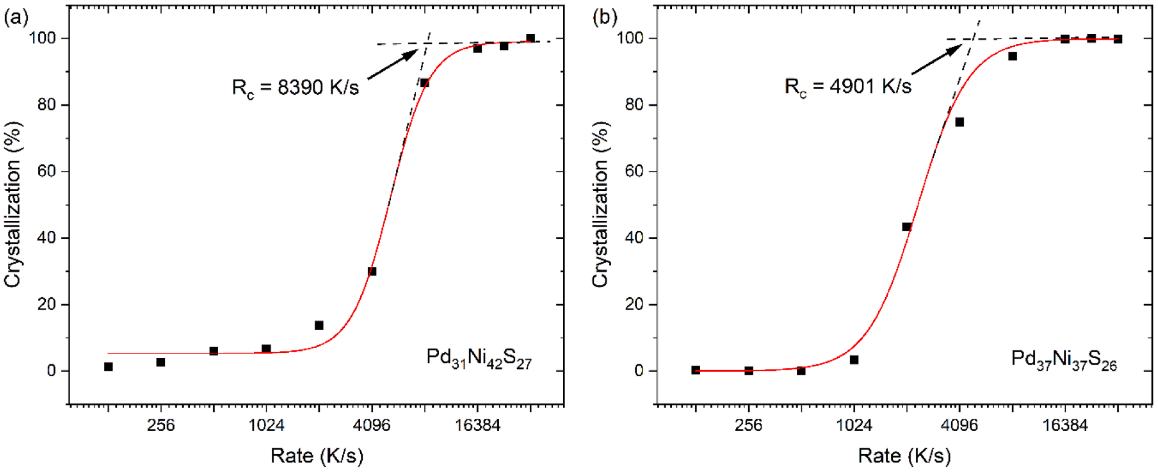

Fig. 6. Changes in Crystallization enthalpy of (a) $Pd_{31}Ni_{42}S_{27}$ and (b) $Pd_{37}Ni_{37}S_{26}$ over a logarithmic cooling rate. Each enthalpy measurement was conducted under a constant heating rate of 100 K s^{-1} following an initial cooling from a temperature significantly above the liquidus temperature of the respective alloy. The point at which the plateau value in crystallization enthalpy is reached signifies the range where fully amorphous samples were achieved, indicating that the critical cooling rate was exceeded.

temperature of a prototyped Au-based metallic melt is 192 K above its liquidus temperature. For this reason, we tried different overheating up to 200 K above the liquidus temperature and holding times ranging from 0.1 s to 10 s to achieve the best result. However, there was a minimal discrepancy in the outcomes obtained at various annealing temperatures, signifying the uncomplicated nature of the melt and implying a lack of substantial overheating requirement.

From Fig. 6, the required CCR for achieving a constant crystallization enthalpy (100 %), indicating an initially fully amorphous sample, is about 8390 and 4901 K s^{-1} for the examined $Pd_{31}Ni_{42}S_{27}$ and $Pd_{37}Ni_{37}S_{26}$ compositions respectively, and is determined from the intersection of the two guiding lines of the plateau and the slope. The calculated critical cooling rate (CCR) can be compared to the macroscopic critical casting thickness d_c using the empirical formula [61], $R_c = \frac{10}{d_c^2}\ K\ cm^2 s^{-1}$ (8), where R_c is the CCR in K s^{-1} and d_c is the critical casting thickness in cm. Considering the experimental d_c of 2 mm in the case of $Pd_{37}Ni_{37}S_{26}$ and 1.5 mm for $Pd_{31}Ni_{42}S_{27}$ [15], an R_c of 250 K s^{-1} for the $Pd_{37}Ni_{37}S_{26}$ and 444 K s^{-1} for the $Pd_{31}Ni_{42}S_{27}$ would be estimated. Although the calculated R_c values exhibit a qualitative trend relative to the critical d_c values, the determination of the CCR using FDSC does not directly correlate with the macroscopic glass-forming ability when applying the established formula based on the experimental critical thickness data. This discrepancy is detected in Au-based BMGs as well [62,63], which has been attributed to the high surface/volume ratio for small-scale samples, and the easy crystallization at the surface [64,65]. However, in the case of Pd-Ni-S system, the volatile sulfur is already a potential source of change in the liquid's composition, affecting their CCR strongly.

3.3. Crystallization of the undercooled liquid

3.3.1. Aerodynamic levitation study

Based on Karup-Moller study [16], the selected Pd-Ni-S variations are located within the ternary phase field of the fcc (Pd,Ni) solid solution, and the binary intermetallic compounds of Pd_4S and Ni_3S_2 at 673 K (below their eutectic melting point). Therefore, one of these phases is expected to form first as the primary crystalline phase during cooling experiments. This is confirmed by the in-situ WAXS experiments, where the diffraction pattern of these equilibrium phases was simulated using the Vesta software [34] and compared to the obtained data and no metastable phases could be identified. The recorded solidification behavior is compared with the Scheil simulations. One example using composition $Pd_{33.5}Ni_{40.5}S_{26}$ is shown in Fig. 7. The CALPHAD calculation shows that first during primary crystallization only small amounts of (Pd, Ni) solid solution are formed down to about 744 K, then co-precipitation with Ni_3S_2 takes place as the temperature decreases down to about 736 K, followed by the formation of Pd_4S. This sequence, in such a small temperature interval of <20 K, is hard to resolve in the synchrotron measurement. Therefore, the synchrotron spectra, detects the formation of all crystalline phases at the same time, which is accompanied by a large heat release due to recalescence, increasing the detected temperature from 707 K to 730 K. The temperature is also shifted to lower temperatures by about 50 K compared to the Scheil simulations, as a result of the undercooling caused by the high cooling rate and the containerless processing condition in the levitation device. However, the achieved cooling rate is not yet as high as the attainable rate in ultra-fast calorimetry. It is important to note that the Scheil simulation is purely thermodynamic and does not account for kinetic aspects, such as undercooling due to rapid cooling, which can alter the phase formation sequence (see Section 4.2, Fig. 11).

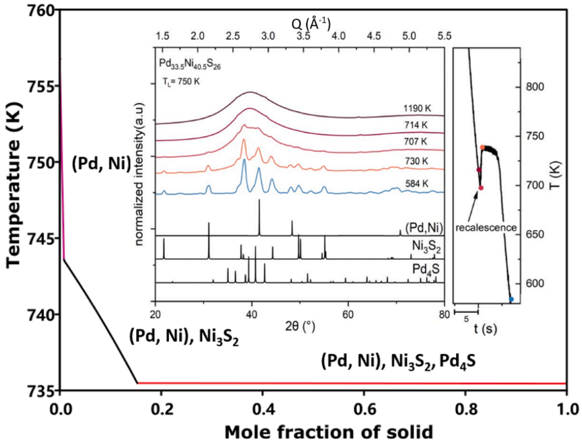

Fig. 7. Scheil solidification simulation for $Pd_{33.5}Ni_{40.5}S_{26}$ in comparison with the in-situ WAXS measurement at 200 K/s cooling rate which shows a heat release due to recalescence, increasing sample's temperature from 707 k to 730 K. The simulated diffraction patterns of the crystalline equilibrium phases including (Pd, Ni) solid solution, Ni_3S_2, and Pd_4S are shown and used to detect the forming phases. All phases start to appear once recalescence sets in.

Regarding the degree of oxidation occurring in ADL, it is acknowledged that aerodynamic levitation does not achieve as high a vacuum level as electrostatic levitation. Consequently, a certain degree of oxidation was observed in some samples (two crystalline peaks at about $q = 3\ \dot{A}^{-1}$ and $4.25\ \dot{A}^{-1}$ in Fig. 7). However, the level of oxidation was not significant enough to alter the phase formation. This conclusion is supported by the fact that a wide range of compositions (off-eutectic compositions, with a clear first phase formation) was analyzed, and the resulting data consistently matched the Scheil-predicted phase formation sequence. It should be noted that the levitation setup is unsuitable for estimating phase fractions based on diffraction peak intensity due to two key factors. First, the large grain size of solidified phases, comparable to the beam size, can cause texture effects that influence peak intensity. Second, the sample, being larger than the beam and partially covered by the nozzle, is not fully illuminated. While the setup is effective for identifying phases and their formation sequences for CALPHAD analysis, it cannot reliably determine phase fractions, particularly given the structural differences between liquid and solid phases.The data for other compositions can be found in the supplementary material.

3.3.2. Time-Temperature-Transformation (TTT) diagrams

In-situ examination of crystallization behavior is conducted using Fast Differential Scanning Calorimetry (FDSC) through isothermal measurements, enabling the recording of Time-Temperature-Transformation (TTT) diagrams for the transformation kinetics of an undercooled metallic melt into the crystalline state. Via very fast cooling rates provided by FDSC, comprehensive examination of TTT diagrams, especially at the nose region, has become achievable for a variety of bulk metallic glasses [23,63,66]. The isothermal TTT diagrams of the $Pd_{31}Ni_{42}S_{27}$, $Pd_{33.5}Ni_{40.5}S_{26}$, and $Pd_{37}Ni_{37}S_{26}$ are depicted in Fig. 8. In the case of measured compositions, the change of annealing temperatures and holding times does not affect the crystallization times significantly, however, longer holding times lead to a faster deterioration of the sample due to the sulfur evaporation. Each isotherm was measured at least three times to ensure reliability. Especially at high temperatures above the nose and the minimum crystallization time, due to the nucleation-controlled crystallization, more statistics are needed. At this high-temperature range, the crystalline growth rate has its maximum and in the case of the formation of a supercritical nucleus, the sample would experience a rapid and short crystallization in a large timescale, resulting in a large scatter of crystallization times at high temperatures.

By integrating the area underneath the exothermal crystallization event in each isothermal measurement, the times at which 1 %, 50 %, and 99 % of the heat release occurred, are determined. In Fig. 8, only the crystallization time of 1 % is shown for the measured compositions, which shows the typical C-shape of TTT diagrams. These data are used for the fitted lines, using the Johnson-Mehl-Avrami-Kolmogorov

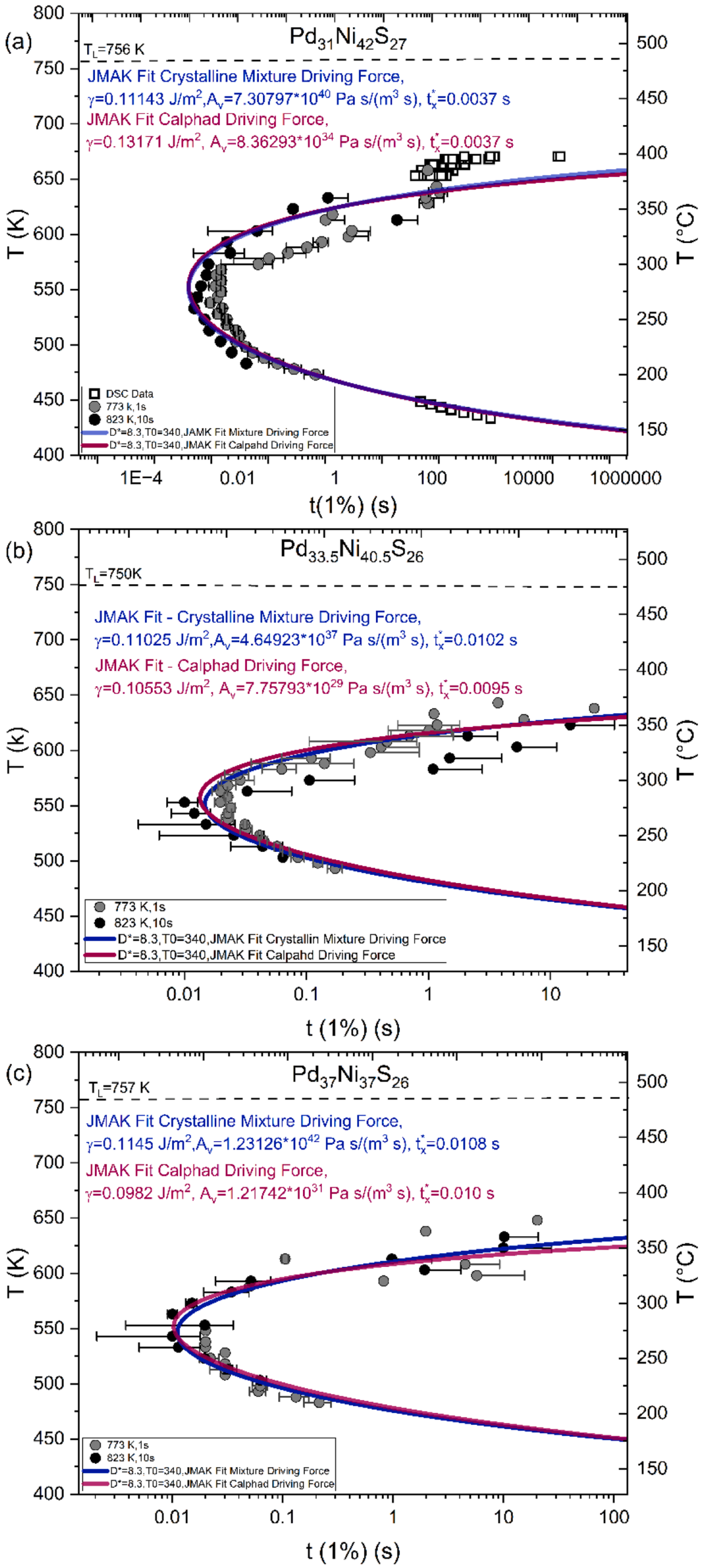

Fig. 8. Isothermal Time–Temperature-Transformation (TTT) diagram of (a) $Pd_{31}Ni_{42}S_{27}$, (b) $Pd_{33.5}Ni_{40.5}S_{26}$, and (c) $Pd_{37}Ni_{37}S_{26}$ determined in fast differential scanning calorimetry (FDSC) (circles) and conventional DSC (squares) for $Pd_{31}Ni_{42}S_{27}$ from [67]. The dark blue and crimson curves show the Johnson–Mehl–Avrami fitting of the experimental data using experimentally determined crystalline mixture driving force and CALPHAD driving force, respectively.

equation (Eq. (11)), presenting a successful fit like what has been observed in previous studies [63,66,68,69] which confirms the homogenous nucleation in the stuided compositions. A detailed discussion on these fits is provided later in the discussion section.

For $Pd_{31}Ni_{42}S_{27,}$ the isothermal crystallization data acquired in a conventional DSC (Perkin Elmer DSC 8500) during heating from the glassy state and cooling from the stable liquid state from Kuball's work [17] is also added to the TTT diagram with square symbols. The DSC data measured at longer times and lower temperatures, as well as higher temperatures in regards to the FDSC data, are in good agreement with the crystallization times measured by FDSC. Such a good compatibility has already been reported in other studies [63,70], and proves the accuracy of measurements.

4. Discussion

4.1. *Gibbs free energy and driving force for crystallization*

4.1.1. *Experimental approach*

In the absence of CALPHAD calculations, we usually determine the Gibbs free energy difference between the undercooled liquid and the crystalline mixture using Eq. (1-7) as described above and use these calculations as an estimate for the driving force. In Fig. 9, the calculated Gibbs free energy curves for Pd-Ni-S variations as a function of temperature, normalized to the liquidus temperature, are compared. They reveal that the Gibbs free energy difference at the glass transition temperature is very similar for all compositional variations, with $Pd_{37}Ni_{37}S_{26}$ exhibiting the smallest value. The compositional dependence of ΔG^{l-x} follows the changes of the enthalpy and entropy of fusion ΔS_m in the system (Table 1), since the variations in heat capacities (Fig. 3 and SI Figure 2) are not that great. This has been already seen in other Au, Pt, Pd, and Zr-based systems [41,71,72].

Compared to other better Pd-based glass-forming alloys such as $Pd_{43}Ni_{10}Cu_{27}P_{20}$ [21] and $Pd_{40}Ni_{40}P_{20}$ [73], Pd-Ni-S alloy variations show a higher entropy of fusion and thus a higher Gibbs free energy difference between the undercooled liquid and the crystalline mixture, explaining their poorer glass-forming ability. However, as mentioned above the Gibbs free energy difference shown in Fig. 9 is only an estimate of the real driving force for crystallization. As depicted schematically in Fig. 10 for a binary A-B system, the calculated ΔG^{l-x} using Eq. (7) in a multiphase system, always refers to the Gibbs free energy difference between the (undercooled) liquid and the crystalline mixture, since $\Delta H_m$and ΔS_m are derived from the melting process of the crystalline mixture and $c_p^x(T)$ is also the measured specific heat capacity of the crystalline mixture. Hence, it is important to note that the Gibbs free energy difference between the liquid and the crystalline mixture is only a lower limit for the driving force for the primary crystallization. The actual driving force for nucleation is correlated to the changes in the chemical potential of the system, if nuclei of a certain crystalline phase are formed [74]. As in Fig. 10, the driving force for the formation of a nucleus of the α-phase is calculated by the parallel tangent construction (black dashed lines) [18]. Therefore, the vertical distance between the two tangents, $\Delta\mu_A^{L-\alpha}$, represents the real driving force for the nucleation of a primary α-nucleus with the composition $X_n(T)$ from the liquid with the composition X_q. From Fig. 10, for a composition at X_q at $T < T_{eut}$ in a binary A-B system, it is evident that ΔG^{l-x} only gives an approximation of the driving force (lower bound) for the formation of a crystalline nucleus [75]. This illustrates the general need for our CALPHAD approach, which is capable of calculating the more realistic driving force for the crystallization of the first-appearing crystalline phase.

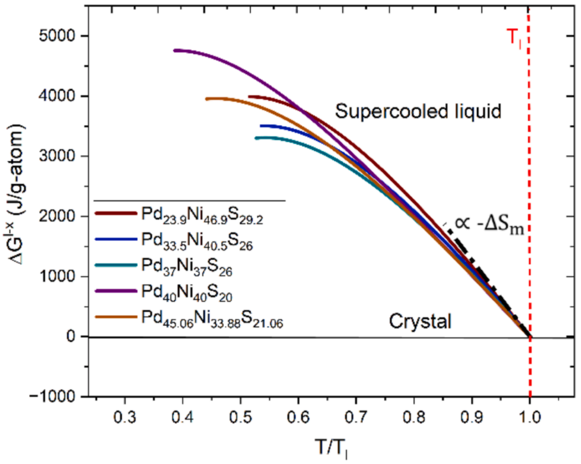

Fig. 9. Calculated Gibbs free energy function with respect to the crystalline state from Eq. (7) for the selected compositions. The slope of ΔG^{l-x} at T_l is proportional to $-\ \Delta S_m$.

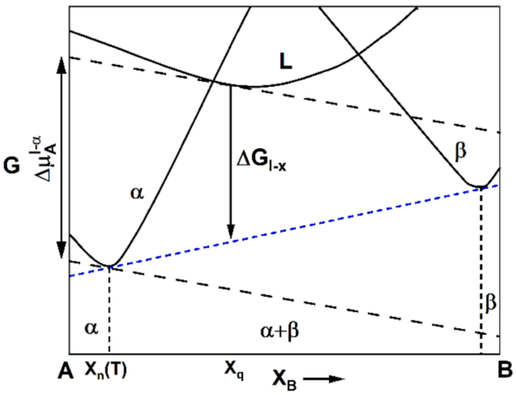

Fig. 10. Schematic Gibbs free energy curves for the competing phases for a nominal composition of X_q at $T<T_{eut}$ in a binary A-B system. $\boldsymbol{\Delta G^{l-x}}$ is the Gibbs free energy difference between the liquid and the crystalline mixture $(\boldsymbol{\alpha} + \boldsymbol{\beta})$. $\boldsymbol{\Delta\mu_A^{L-\alpha}}$ is the actual driving force for the nucleation of an $\boldsymbol{\alpha}$-nucleus of the composition $\boldsymbol{X_n}(\boldsymbol{T})$ within the liquid with the composition $\boldsymbol{X_q}$ [75]. Therefore $\boldsymbol{\Delta G^{l-x}}$ is genelly underestimating the driving force for primary crystallization and can be considered a lower bound.

4.2. *CALPHAD approach*

The driving force for the crystallization of each crystalline equilibrium phase from the undercooled liquid can be determined from the CALPHAD calculations. This assessment spans across temperatures from the liquidus temperature down to the glass transition temperature, employing the double tangent construction method as depicted schematically in Fig. 10. The driving force of the phase transformation is defined by the vertical distance between the tangent to the metastable liquid state (L) and the tangent line at the lowest lying equilibrium state (α in case of Fig. 10).

Fig. 11 shows the CALPHAD calculations of the driving force for crystallization of all three competing crystalline phases for $Pd_{23.9}Ni_{46.9}S_{29.2}$, $Pd_{31}Ni_{42}S_{27}$, $Pd_{33.5}Ni_{40.5}S_{26}$, $Pd_{37}Ni_{37}S_{26}$, $Pd_{40}Ni_{40}S_{20}$, and $Pd_{45.1}Ni_{33.9}S_{21.1}$ liquid. Additionally, the experimentally determined Gibbs free energy of the crystalline mixture is included (black curve) for comparison. Discrepancies in the initial points of the driving forces are observed, likely stemming from the incongruent melting behavior of multi-component alloys and varying assumptions between experimental and modeling approaches. When a certain level of undercooling of about 0.8 T_m (see TTT-diagrams in Fig. 8) necessary for homogenous nucleation [76] is maintained during the cooling process, and the undercooled liquid remains homogeneous with the same composition as the high-temperature liquid, the initial phase to form will consistently be the one with the highest driving force at that

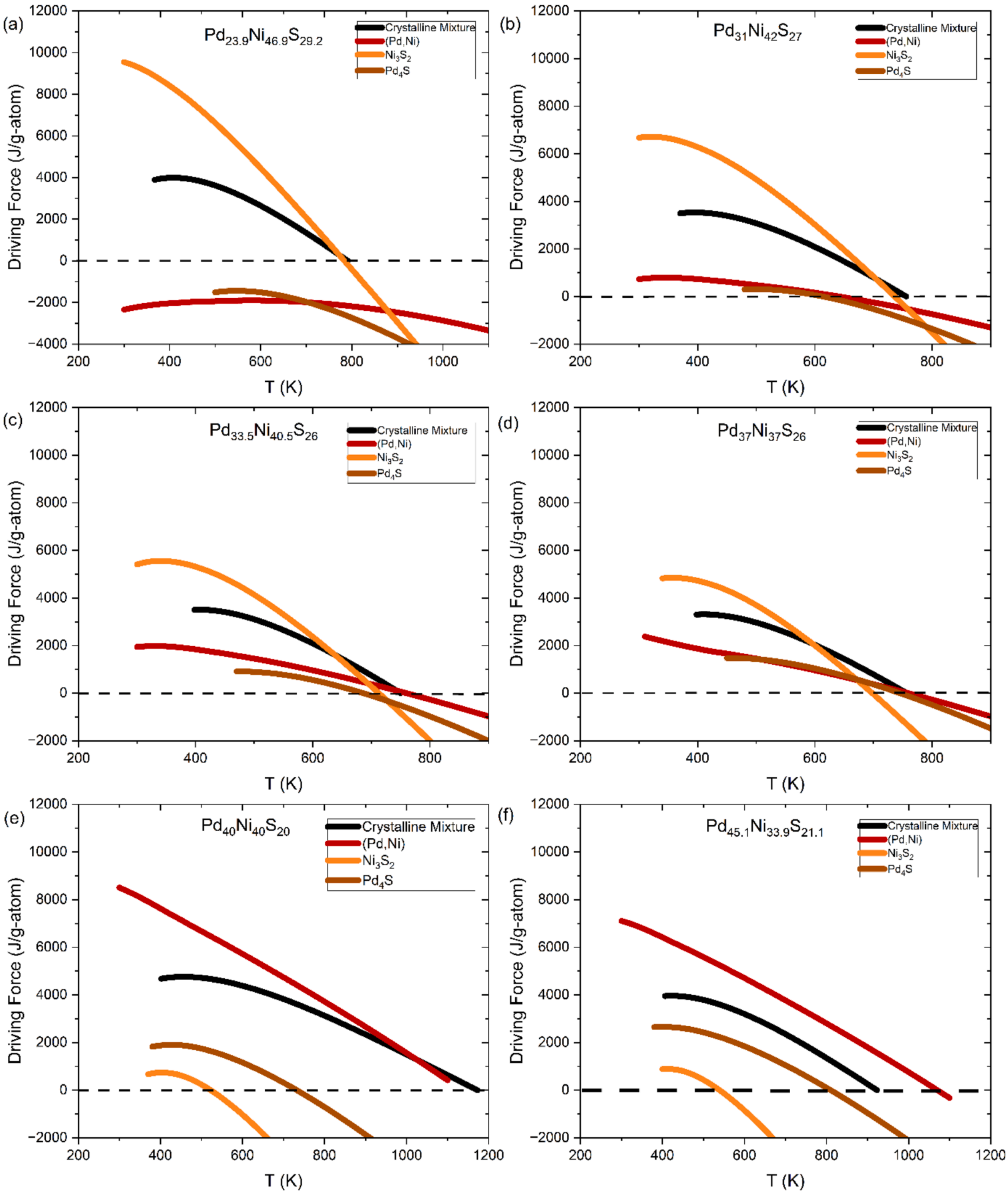

Fig. 11. Calculated driving forces, $\Delta\mu^{l\text{-}i}$ (for phase i), for crystallization of all the crystalline phases that compete with the undercooled liquid for (a) $Pd_{23.9}Ni_{46.9}S_{29.2}$, (b) $Pd_{31}Ni_{42}S_{27}$, (c) $Pd_{33.5}Ni_{40.5}S_{26}$, (d) $Pd_{37}Ni_{37}S_{26}$, (e) $Pd_{40}Ni_{40}S_{20}$, and (f) $Pd_{45.1}Ni_{33.9}S_{21.1}$ in comparison with the calculated $\boldsymbol{\Delta G^{l-x}}$ between the undercooled liquid and the crystalline mixture. Close to the eutectic (c,d) the prediction for primary crystallization from the crystalline mixture, $\Delta G^{l\text{-}x}$, and the CALPHAD calculation $\Delta\mu^{l\text{-}i}$ in the relevant temperature range from about 550 K to 625 K (see Fig. 8) are close. In the off-eutectic cases (a,b, e, f) the crystalline mixture underestimates the driving force as it has been illustrated in Fig. 10.

temperature. For compositions starting with $Pd_{23.9}Ni_{46.9}S_{29.2}$ from the Ni_3S_2 side and going towards the eutectic point, Ni_3S_2 emerges as the primary phase. As previously discussed, here we could see the clear difference between the actual driving force calculated by CALPHAD and the calculated Gibbs free energy difference from the experimental data for all the compositions, which becomes smaller as we approach the eutectic point. This shows that our experimental approach is a good approximation tool for near-eutectic compositions, however in the case of off-eutectic compositions, one should be more careful as the discrepancies get bigger. This holds significance in the TTT diagram, where Ni_3S_2 is anticipated to form after rapid cooling and the sample's isothermal holding at the respective temperature. Subsequently, the interfacial energy related to this phase will be determined by employing the calculated driving forces within the Johnson-Mehl-Avrami-Kolmgrov (JMAK) fit (Eq. (11)) of the experimental crystallization times. In the case of $Pd_{40}Ni_{40}S_{20}$, and $Pd_{45.1}Ni_{33.9}S_{21.1}$, it is evident that (Pd,Ni) solid solution is significantly more stable compared to the other phases and is expected to form as the primary phase which is consistent with the HEXRD observations (see SI Figure 1 and 4).

4.3. Fragility estimations

To properly describe the TTT diagrams, measured in the framework of this study as plotted in Fig. 8, the kinetics of the undercooled liquid need to be estimated. In terms of kinetics, the fragility of the liquid phase, as classified by Angell, plays a pivotal role in glass formation [77, 78]. This property describes the rate at which viscosity or structural relaxation time (τ) varies with temperature. Determining fragility involves fitting equilibrium viscosity $\eta(\mathrm{T})$ or α-relaxation time data $\tau(\mathrm{T})$ to Angell's proposed form of the empirical Vogel-Fulcher-Tammann relation [78]

$$\mathrm{x(T)} = \mathrm{x_0 exp}\left(\frac{\mathrm{D^* T_0}}{T - \mathrm{T_0}}\right), \tag{9}$$

where D^* is the fragility parameter showing the derivation from Arrhenius behavior and T_0 is the VFT temperature, where the x(T) (being either η or τ) diverges, and the pre-exponential factor $\mathrm{x_0}$, represents the minimum value of x(T) at infinitely high temperatures. In this relation, liquids with a large D^* showing Arrhenius-like temperature dependence are termed strong, and the ones with a small D^* showing rather super-Arrhenius-like behavior are known as fragile liquids. Fragile liquids tend to have faster kinetics at temperatures, where the nose of the TTT diagram is located, leading to shorter crystallization times at the nose.

Using the m -fragility approach, it's possible to quantify fragility based on the curve steepness of the investigated quantity $x(T)$ in an Angell plot at $T_g^*/T = 1$ (T_g^* is defined by the Temperature at which $\eta = 10^{12} Pa\ s$) [79]

$$m = \frac{\partial log_{10}(x(T))}{\partial \frac{T_g^*}{T}}. \tag{10}$$

where higher m values are indicator of a higher temperature sensitivity of the $x(T)$ around T_g and a more fragile liquid. Fig. 12(a) shows $\log_{10}(\tau_\mathrm{d})$ of the $Pd_{31}Ni_{42}S_{27}$, $Pd_{33.5}Ni_{40.5}S_{26}$ and $Pd_{37}Ni_{37}S_{26}$ liquid, measured at a base frequency of 10 Hz using the step response analysis method, normalized to T^*/T. As shown in [80], obtaining the exact τ_0 value for a particular liquid is challenging, leading to uncertainty regarding the comparability of Vogel-Fulcher-Tammann (VFT) fits across different systems within the timescale regime. To circumvent these challenges, m -fragilities are determined by conducting linear Arrhenius-like fits of $log_{10}(\tau_d)$ data [80], as shown in Fig. 12(a). The respective fits are shown in an Angell type plot, using the maximum $log_{10}(\tau_d)$ data point which is the same for all three compositions, to define T^* and have a qualitative comparison of m_τ.

As depicted in Fig. 12(a), the linear fitted lines seem satisfactory, as the overall super-Arrhenius temperature dependence of τ_d can be deemed negligible over such a short temperature range. The calculated m -fragilities for $Pd_{31}Ni_{42}S_{27}$, $Pd_{33.5}Ni_{40.5}S_{26}$, and $Pd_{37}Ni_{37}S_{26}$ are 53.5, 51.2, and 39.6 respectively. Based on these results, $Pd_{33.5}Ni_{40.5}S_{26}$ is found to be a slightly stronger system, while $Pd_{31}Ni_{42}S_{27}$ and $Pd_{37}Ni_{37}S_{26}$ show very close m_τ values indicating their similar fragilities.

Another fragility estimation approach uses the connection between kinetic and thermodynamic properties to quantitatively determine the thermodynamic fragility [21,81]. As shown by molecular dynamics simulations [82], the deeply supercooled liquid undergoes structural redistribution and ordering processes, resulting in significant variations in the specific heat capacity near the glass transition temperature. Based on Adam- Gibbs theory [83], as the liquid is further undercooled, the so-called cooperatively rearranging regions (CRRs) formed by groups of atoms grow in size and increase their degree of cooperativity. As a result, the number of available configurations within the system decreases, leading to a decrease in configurational entropy S_c. This decrease is accompanied by an increased specific heat capacity, which is linked to the significant rise in viscosity and relaxation times as the glass transition is approached. Assuming a negligible difference in vibrational entropy between the liquid and crystalline states [49], the excess entropy (entropy difference between undercooled liquid and crystalline state), ΔS^{l-x}, can be employed instead of S_c to estimate the entropic changes with temperature.

A qualitative connection between the concept of kinetic fragility and excess entropy was proposed by Angell et.al [82,84], in which instead of relying on relaxation time or viscosity, they utilized the change in configurational entropy or excess entropy around the glass transition to describe thermodynamic fragility. In this approach, considering $\frac{\mathrm{d}\Delta \mathrm{S}^{l-x}}{\mathrm{dT}} = \frac{\Delta \mathrm{c}_\mathrm{p}^{l-x}}{\mathrm{T}}$, and with the assumption $\Delta \mathrm{C}_\mathrm{p}^{l-x}(\mathrm{T_g}) \approx \Delta \mathrm{C}_\mathrm{p}^{l-g}(\mathrm{T_g})$, the difference in isobaric specific heat capacity between liquid and crystal $\Delta \mathrm{C}_\mathrm{p}^{l-x}(\mathrm{T_g})$ at the glass transition temperature can be used as a tool for determination of thermodynamic fragility, where a larger jump in specific heat capacity at glass transition indicates a more rapid increase of configurational entropy in the liquid upon cooling and a more thermodynamically fragile behavior. Afterwards, by using the relations $m = 40\ \frac{\Delta \mathrm{C}_\mathrm{p}^{l-x}(\mathrm{T_g})}{\Delta \mathrm{S_m}}$ [85], and $m = 17 + \frac{590}{\mathrm{D^*}}$ [86], the thermodynamic fragility and kinetic fragility can be connected, and D^* can be approximated. Fig. 12(b) depicts the developments in the reversed isobaric specific heat capacity between liquid and crystal $\Delta \mathrm{C}_\mathrm{p}^{l-x}(\mathrm{T_g})$ as a function of composition

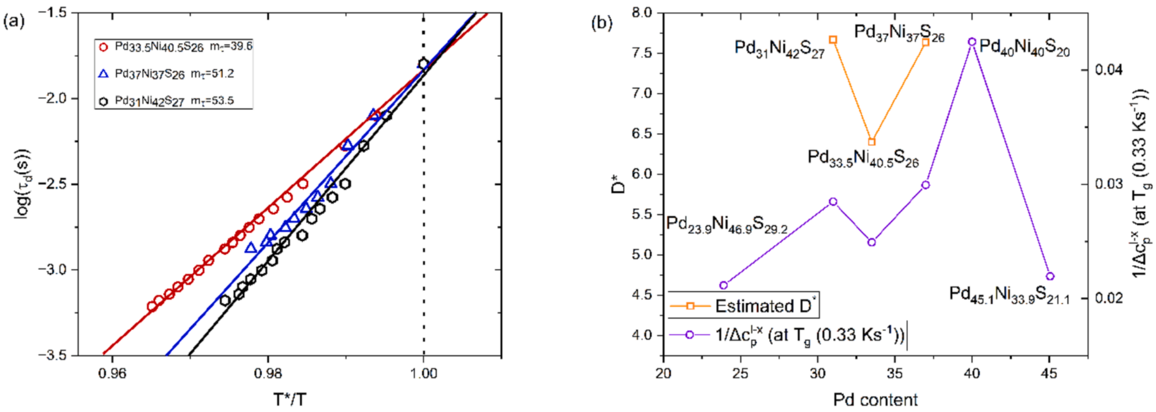

Fig. 12. Fragility estimations. (a) Linear Arrhenius fits of τ_d (T) in an Angell-type graph for all three compositions. The linear fits are done with regard to the maximum $log_{10}(\tau_d)$ data point which is the same for all three compositions to define T^* and the m -fragility (m_τ). (b) Changes in $1/\Delta \mathrm{C}_\mathrm{p}^{l-x}(\mathrm{T_g})$ as a function of composition (Pd content) together with the approximated kinetic fragility parameter D^* plotted for all Pd-Ni-S alloy variations.

together with the approximated fragility parameter D^*. As can be seen, D^* and $1/\Delta c_p^{l-x}(T_g)$ show the same trend for all the compositions, as the decrease in $\Delta c_p^{l-x}(T_g)$ (increase in $1/\Delta c_p^{l-x}(T_g)$) translates into a higher fragility parameter (D^*).

For the three better glass-forming compositions, $Pd_{31}Ni_{42}S_{27}$, $Pd_{33.5}Ni_{40.5}S_{26}$, and $Pd_{37}Ni_{37}S_{26}$ the estimated D^* is in the same range from 6.5 to 7.5, indicating their comparable behavior, while $Pd_{23.9}Ni_{46.9}S_{29.2}$ and $Pd_{45.1}Ni_{33.9}S_{21.1}$ show a more fragile behavior with a D^* of 5.5 and 4 respectively. However, overall, the low D^* range observed in Pd-Ni-S variations suggests a rather fragile kinetic behavior, as D^* values of bulk glass-forming liquids typically range from 10 to 26 [21,40,46,56,87], where a higher D^* value signifies a higher viscosity at the melting point and at the nose of the TTT diagram for crystallization, which leads to a higher glass-forming ability (GFA). Given the large driving force for crystallization and the fragile liquid behavior observed in these compositions, the formation of bulk glass with a critical diameter (d_c) of at least 1 mm in the Pd-Ni-S system seems unlikely and is rather noteworthy. Therefore, the glass-forming ability (GFA) in this system can be attributed to a high interfacial energy between the liquid and crystalline mixture, which results in a significant decrease in the nucleation rate, similar to the case observed in Pt-P based liquids [69]. This aspect is further examined in the following section.

4.4. Interfacial energy calculation

In addition to the driving force and viscosity, another critical factor influencing crystallization kinetics is the energy barrier that must be overcome to form a stable nucleus, which can grow into a crystal. For a spherical nucleus in classical nucleation theory, the nucleation barrier, ΔG^*, is related to the interfacial energy and the excess Gibbs free energy by the relation $\Delta G^*(T) \sim \gamma_{l-x}^3/\Delta G(T)_{l-x}^2$, where γ_{l-x} represents the interfacial energy between liquid and crystal. According to this relation, a high interfacial energy also promotes glass formation by raising the nucleation barrier in addition to a low driving force.

The interfacial energy between the nucleating crystal and liquid can be approximated as a fitting parameter within the Johnson-Mehl-Avrami-Kolmogorov (JMAK) equation. Based on classical nucleation theory and steady-state nucleation, the time required to crystallize a volume fraction of x (e.g. 1, 50, 99 %) during isothermal annealing can be modeled via [74]

$$t(T) = \left(-3\ln(1-x)/(\pi I_v(T)[u(T)]^3)\right)^{1/4}, \tag{11}$$

in which $I_v(T) = A_v/\eta(T)\exp\left(-16\pi\gamma_{l-x}/\left(3k_bT[\Delta G_{l-x}(T)]^2\right)\right)$ and $u(T) = fk_bT/(3\pi a_0{}^2\ \eta(T)[1-\exp(n\Delta G_{l-x}(T)/(k_bT))]$ are the crystal nucleation rate per unit volume and the crystal growth rate, respectively. In these equations, A_v is a fitting parameter, k_b the Bolzmann constant, a_0 the average atomic diameter, n the average atomic volume, and $\Delta G_{l-x}(T)$ is the volumetric free energy difference between liquid and crystal driven from Eq. (7). The atomic – scale roughness of the liquid-crystal interface is represented by the prefactor, f, which is considered to be unity in our case with $\Delta S_m = \Delta H_m/T_l < 2R$ (rough interface) for the solidification of metals. The prefactor would be calculated as $0.2\ (T-T_l)/T_l$ in the case of $\Delta S_m = \Delta H_m/T_l < 4R$ (smooth interface) [88]. The Vogel–Fulcher–Tammann (VFT) Eq. (9) is used to describe the $\eta(T)$ function after fitting to experimental equilibrium viscosity or relaxation times. Since these compositions show very similar fragilities as shown in Section 4.3, the derived parameters from the VFT fit by Kuball et al. [17] for the best glass-forming composition, $Pd_{31}Ni_{42}S_{27}$, were used to describe the kinetics of all three compositions.

Fig. 8 shows the experimentally determined times, at which 1 % of the sample has isothermally crystallized (circles) in the temperature range that is experimentally accessible. In addition, two fits to the data with the JMAK equation (Eq. (11)) for all three compositions are shown. One uses the calculated Gibbs free energy difference between the supercooled liquid and the crystalline mixture from Eq. (7) (dark blue curves) and the other (crimson curves) utilizes the calculated driving force from CALPHAD modeling for the primary phase as shown in Fig. 11. The approximated interfacial energies through both fitting approaches and the minimum crystallization time driven from the fitted curve,the so-called nose time $t_x^*(s)$, are summarized in Table 3. The JMAK fitting, employing the calculated driving force from CALPHAD modeling, exhibits more or less the same fit for these compositions, showing a slightly better match to the experimental data at the nose of the crystallization. This slight improvement in the fit can be attributed to considering the actual driving force associated with the initial phase formation (Ni_3S_2), thereby aligning more accurately with the experimental data. Nevertheless, the obtained results suggest that the earlier approach, which involved considering the Gibbs free energy of the crystalline mixture, estimates an interfacial energy value very close to the interfacial energy value obtained, when using the driving force from the CALPHAD calculations. The reason is, that for all three compositions close to the eutectic, the driving forces for all crystalline phases are very similar slightly below their melting point (Fig. 11), so they all crystallize virtually simultaneously (inset in Fig. 7).

However, in the case of off-eutectic compositions, CALPHAD calculations' role becomes more crucial. As one moves away from the eutectic point, the driving force for primary crystallization increases, and the disparity between the experimentally determined Gibbs free energy difference between the supercooled liquid and the crystalline mixture and the actual (CALPHAD) driving force increases, which impacts the estimation of the interfacial energy significantly. This is the case in Fig. 11(a) for the $Pd_{23.9}Ni_{46.9}S_{29.2}$. This plot clearly shows that the actual driving force for the formation of Ni_3S_2 phase is much larger than the estimation from the crystalline mixture and by approaching the eutectic point the disparity decreases. Unfortunately for the composition $Pd_{23.9}Ni_{46.9}S_{29.2}$ the time scale for crystallization is too short to measure the TTT diagram even in the Flash DSC and a comparison between real driving force and Gibb free energy of the crystalline mixture is not possible.

For all three compositions presented in Table 3, the estimated interfacial energy values, derived using the driving force of crystalline mixture, are quite similar. This similarity is not surprising, based on the fact that the driving forces of the crystalline mixture are also closely aligned (Fig. 9),and that the measured TTT diagrams are very similar resulting in close interfacial energies derived as a fitting parameter. However, the interfacial free energy at the solid-liquid interface very much depends on the local orders in the liquid and solid, along with the thermodynamics. For the three liquid compositions in question, the crystalline phase that nucleates first is the same (Ni_3S_2), but the composition difference across the interface between the liquid and the crystal that forms first, is different. This is why in reality the interfacial energy should be different. Therefore, when we use CALPHAD driving forces, the resulting fitted interfacial energies should be closer to the real value, which unfortunately cannot be determined experimentally. These real interfacial energies show a slight variation in concentration indicating that the composition difference between liquid and primary crystal cannot be neglected.

At the liquidus temperature (T_l), the solid and liquid phases are in equilibrium, where the high enthalpy of the liquid is balanced by its high entropy, leading to equal chemical potentials for both liquid and solid phases. However, this balance is disrupted at the interface resulting in an excess free energy, denoted as γ_{sl}. Hence, by the formation of a solid sphere, the solidified sphere and liquid must then have the same chemical potential. From Gibbs- Thomson effect, $\Delta G_v = 2\gamma_{sl}/r^*$, where r^* is the radius of the solid sphere in (unstable) equilibrium with the surrounding liquid and ΔG_v is the free energy difference of solid and liquid per unit volume, a solid sphere of radius r will have a free energy greater than that of the stable bulk solid by $2\gamma/r$ per unit volume, and therefore for the nucleation of a specific solid phase with a critical r^*, the

Table 3
JMAK parameters acquired by the fitting procedure.

	Derived from JMAK Fit with crystalline mixture driving force			Derived from JMAK Fit with Ni_3S_2 driving force		
Composition	$t_x^*(s)$	$\gamma\ (J/m^2)$	$A_v\,(Pa/m^3)$	$t_x^*(s)$	$\gamma\ (J/m^2)$	$A_v\,(Pa/m^3)$
$Pd_{31}Ni_{42}S_{27}$	0.0037	0.11143	7.30797×10^{40}	0.0037	0.13171	8.36239×10^{34}
$Pd_{33.5}Ni_{40.5}S_{26}$	0.0102	0.11025	4.64923×10^{37}	0.0095	0.10553	7.75793×10^{29}
$Pd_{37}Ni_{37}S_{26}$	0.0108	0.1145	1.23126×10^{42}	0.00982	0.0982	1.21742×10^{31}

Gibbs energy difference between the crystal and liquid, is directly related to the interfacial energy at the interface and varies accordingly [89].

These estimated interfacial energy values are comparable to those determined for Pt-based metallic glasses [69,90], which are considerably higher compared to other glass-forming systems like Zr-based systems [91,92], compensating for the large driving force and the fragile liquid behavior of these glass-forming liquids [69].

Regarding the minimum crystallization time, $t_x^*(s)$, an empirical equation relating the crystallization nose time $t_x^*(s)$ to the critical casting diameter d_c (mm) was developed by Johnson et al. [93] as

$$t_x^*(s) = 0.00419\ (d_c)^{2.54}. \tag{12}$$

This results in a d_c of approximately 1.4 mm for $Pd_{33.5}Ni_{40.5}S_{26}$ and $Pd_{37}Ni_{37}S_{26}$ and 0.95 mm for $Pd_{31}Ni_{42}S_{27}$, which is in good agreement with the experimentally determined d_c of 2 mm and 1.5 mm for $Pd_{37}Ni_{37}S_{26}$ and $Pd_{31}Ni_{42}S_{27}$ compositions, respectively [15].

5. Summary and conclusions

In this work, a comprehensive experimental and computational investigation into the thermo-physical properties of the novel ternary BMG-forming Ni-Pd-S system was conducted. This system was chosen due to its relative simplicity regarding equilibrium thermodynamics and the extensive experimental data on equilibrium phases available in the literature, facilitating the application of the CALPHAD approach for the modeling of the underlying thermodynamics affecting the glass formation.

Using the two-state liquid model, the modeling of the undercooled liquid and glass for the pure elements was done. Further, the model was extended to its corresponding binary and ternary system, where the modeled results were compared with experimental data and optimized accordingly.

Our experimental investigations employed methods such as Differential Scanning Calorimetry (DSC), Differential Thermal Analysis (DTA), and Flash-DSC (chip-calorimetry). Additionally, primary phase formation studies using high-energy synchrotron diffraction experiments (HEXRD) were conducted to compare and validate CALPHAD modeling results.

Using the parallel tangent method for Gibbs free energy in both crystalline and liquid phases, the driving force for crystallization of the possible phases (Ni_3S_2, Pd_4S, and (Pd,Ni) solid solution) within the Pd-Ni-S alloy variations was calculated. This method provided a more precise estimation of the nucleation driving force for the initial phase compared to traditional thermodynamic approaches. The calculated driving forces were then used to model isothermal Time-Temperature-Transformation (TTT) diagrams.

The JMAK fitting, incorporating the driving force derived from CALPHAD modeling, exhibited a comparable fit to the one applied using the crystalline mixture driving force across various compositions with a slight enhancement in alignment at the crystallization nose, attributed to the precise consideration of the driving force during the initial formation of Ni_3S_2.

For compositions near the eutectic point, the driving forces for all crystalline phases were found to be nearly identical, causing them to crystallize almost simultaneously. However, for compositions far from the eutectic point, the importance of CALPHAD calculations increases. As compositions diverge from the eutectic, the driving force for primary crystallization increases, leading to a larger discrepancy between the experimentally determined Gibbs free energy difference and the actual CALPHAD driving force. This significantly impacts the interfacial energy estimation.

The estimated interfacial energy values for all three compositions, derived from the crystalline mixture driving force, were quite similar due to the closely aligned driving forces. When using CALPHAD driving forces, the values showed a slight decline, reflecting the decrease in Ni_3S_2 driving forces as the eutectic point was approached. Both sets of calculated interfacial energies were very close, indicating the good accuracy of our previous method for near eutectic compositions, which considered the Gibbs free energy of the crystalline mixture. These calculated considerably large interfacial energies are capable of offsetting the large driving force and fragile liquid behavior of Pd-Ni-S glass-forming liquids, enabling them to form bulk metallic glasses with a critical diameter (d_c) of at least 1 mm.

In conclusion, our experimental approach remains a valuable tool for understanding and predicting the thermodynamics of glass-forming systems, particularly near eutectic compositions. Furthermore, our CALPHAD approach offers a new and accurate means of calculating the driving force for the crystallization of the primary phase, which is critical for assessing glass-forming ability. These findings highlight the interplay of thermodynamic principles, compositional factors, and advanced modeling techniques in the study of metallic glass formation.

CRediT authorship contribution statement

Maryam Rahimi Chegeni: Writing – original draft, Visualization, Validation, Methodology, Investigation, Formal analysis, Conceptualization. **Wenhao Ma:** Writing – review & editing, Visualization, Validation, Software, Methodology, Investigation, Formal analysis, Conceptualization. **Sascha Sebastian Riegler:** Writing – review & editing, Methodology, Investigation. **Amirhossein Ghavimi:** Writing – review & editing, Methodology, Investigation. **Magnus Rohde:** Supervision, Methodology, Conceptualization. **Fan Yang:** Writing – review & editing, Methodology, Investigation. **Hans Jürgen Seifert:** Supervision, Funding acquisition, Data curation, Conceptualization. **Isabella Gallino:** Writing – review & editing, Supervision, Methodology, Funding acquisition, Data curation, Conceptualization. **Ralf Busch:** Writing – review & editing, Supervision, Methodology, Funding acquisition, Data curation, Conceptualization.

Declaration of competing interest

The authors declare that they have no known competing financial interests or personal relationships that could have appeared to influence the work reported in this paper.

Acknowledgments

This research was funded by the Deutsche Forschungsgemeinschaft (DFG). The authors are grateful to N. Neuber, O. Gross, and M. Frey for their valuable discussions. They also appreciate the opportunity to conduct high-energy synchrotron XRD experiments at Petra III, the light source at the German Electron Synchrotron (DESY) in Hamburg, a member of the Helmholtz Association (HGF). They would also like to thank Maike Becker, Johanna Wilden, and Thomas Werner from DLR, as well as Ann-Christin Dippel and Fernando Igoa Saldaña from DESY, for their support during the beamtime.

Supplementary materials

Supplementary material associated with this article can be found, in the online version, at doi:10.1016/j.actamat.2025.121074.

References

[1] W. Klement, R.H. Willens, P.O.L. Duwez, Non-crystalline structure in solidified gold–Silicon alloys, Nature 187 (1960) 869–870, https://doi.org/10.1038/187869b0.

[2] X.H. Lin, W.L. Johnson, Formation of Ti–Zr–Cu–Ni bulk metallic glasses, J. Appl. Phys. 78 (1995) 6514–6519, https://doi.org/10.1063/1.360537.

[3] C. Suryanarayana, A. Inoue, Iron-based bulk metallic glasses, Int. Mater. Rev. 58 (2013) 131–166, https://doi.org/10.1179/1743280412Y.0000000007.

[4] X. Wang, I. Yoshii, A. Inoue, Y.-H. Kim, I.-B. Kim, Bulk amorphous $\mathrm{Ni}_{75\text{-}x}\mathrm{Nb}_5\mathrm{M}_x\mathrm{P}_{20\text{-}y}\mathrm{B}_y$ (M=Cr, Mo) alloys with large supercooling and high strength, Mater. Trans., JIM 40 (1999) 1130–1136, https://doi.org/10.2320/matertrans1989.40.1130.

[5] A.J. Drehman, A.L. Greer, D. Turnbull, Bulk formation of a metallic glass: pd40Ni40P20, Appl. Phys. Lett. 41 (1982) 716–717, https://doi.org/10.1063/1.93645.

[6] Y.C. Kim, W.T. Kim, D.H. Kim, A development of Ti-based bulk metallic glass, Mater. Sci. Eng.: A 375–377 (2004) 127–135, https://doi.org/10.1016/j.msea.2003.10.115.

[7] A. Peker, W.L. Johnson, A highly processable metallic glass: zr41.2Ti13.8Cu12.5Ni10.0Be22.5, Appl. Phys. Lett. 63 (1993) 2342–2344, https://doi.org/10.1063/1.110520.

[8] P.J. Spencer, The origins, growth and current industrial impact of Calphad, CALPHAD. 79 (2022) 102489, https://doi.org/10.1016/j.calphad.2022.102489.

[9] M. Palumbo, L. Battezzati, Thermodynamics and kinetics of metallic amorphous phases in the framework of the CALPHAD approach, CALPHAD. 32 (2008) 295–314, https://doi.org/10.1016/j.calphad.2007.12.002.

[10] M. Palumbo, G. Cacciamani, E. Bosco, M. Baricco, Thermodynamic analysis of glass formation in Fe-B system, CALPHAD. 25 (2001) 625–637, https://doi.org/10.1016/S0364-5916(02)00012-3.

[11] R. Bormann, F. Gärtner, K. Zöltzer, Application of the CALPHAD method for the prediction of amorphous phase formation, J. Less Common Metals 145 (1988) 19–29, https://doi.org/10.1016/0022-5088(88)90258-5.

[12] R.B. Schwarz, P. Nash, D. Turnbull, The use of thermodynamic models in the prediction of the glass-forming range of binary alloys, J. Mater. Res. 2 (1987) 456–460, https://doi.org/10.1557/JMR.1987.0456.

[13] S. Bigdeli, H. Mao, M. Selleby, On the third-generation Calphad databases: an updated description of Mn, Phys. Status Solidi(b) 252 (2015) 2199–2208, https://doi.org/10.1002/pssb.201552203.

[14] J. Agren, B. Cheynet, M.T. Clavaguera-Mora, K. Hack, J. Hertz, F. Sommer, U. Kattner, Thermodynamic models and data for pure elements and other endmembers of solutions: group 2 extrapoliation of the heat capacity in liquid and amorphous phases, CALPHAD. 19 (1995) 449–480.

[15] A. Kuball, B. Bochtler, O. Gross, V. Pacheco, M. Stolpe, S. Hechler, R. Busch, On the bulk glass formation in the ternary Pd-Ni-S system, Acta Mater. 158 (2018) 13–22, https://doi.org/10.1016/j.actamat.2018.07.039.

[16] S. Karup-Moller, E. Makovicky, The system Pd-Ni-S at 900 degrees, 725 degrees, 550 degrees, and 400 °C, Econ. Geol. 88 (1993) 1261–1268, https://doi.org/10.2113/gsecongeo.88.5.1261.

[17] A. Kuball, O. Gross, B. Bochtler, I. Gallino, R. Busch, Thermodynamics, kinetics and crystallization behavior of the Pd31Ni42S27 bulk glass forming alloy, Intermetallics. (Barking) 173 (2024) 108422, https://doi.org/10.1016/j.intermet.2024.108422.

[18] S. Gorsse, G. Orveillon, O.N. Senkov, D.B. Miracle, Thermodynamic analysis of glass-forming ability in a Ca-Mg-Zn ternary alloy system, Phys. Rev. B 73 (2006) 224202, https://doi.org/10.1103/PhysRevB.73.224202.

[19] A. Inoue, N. Nishiyama, H. Kimura, Preparation and thermal stability of bulk amorphous $\mathrm{Pd}_{40}\mathrm{Cu}_{30}\mathrm{Ni}_{10}\mathrm{P}_{20}$ alloy cylinder of 72 mm in diameter, Mater. Trans., JIM 38 (1997) 179–183, https://doi.org/10.2320/matertrans1989.38.179.

[20] R. Busch, W. Liu, W.L. Johnson, Thermodynamics and kinetics of the Mg65Cu25Y10 bulk metallic glass forming liquid, J. Appl. Phys. 83 (1998) 4134–4141, https://doi.org/10.1063/1.367167.

[21] I. Gallino, J. Schroers, R. Busch, Kinetic and thermodynamic studies of the fragility of bulk metallic glass forming liquids, J. Appl. Phys. 108 (2010) 1–8, https://doi.org/10.1063/1.3480805.

[22] O. Haruyama, T. Makimura, T. Miyakawa, K. Sugiyama, A study on chemical short range ordering in Pd40Ni40P20Bulk metallic glass by anomalous X-ray scattering, High Temperat. Mater. Process. 29 (2010) 381–392, https://doi.org/10.1515/HTMP.2010.29.5-6.381.

[23] N. Sohrabi, J.E.K. Schawe, J. Jhabvala, J.F. Löffler, R.E. Logé, Critical crystallization properties of an industrial-grade Zr-based metallic glass used in additive manufacturing, Scr. Mater. 199 (2021) 113861, https://doi.org/10.1016/j.scriptamat.2021.113861.

[24] S. Pogatscher, D. Leutenegger, A. Hagmann, P.J. Uggowitzer, J.F. Löffler, Reprint of: characterization of bulk metallic glasses via fast differential scanning calorimetry, Thermochim. Acta 590 (2014) 46–52, https://doi.org/10.1016/j.tca.2014.12.012.

[25] J.Q. Wang, Y. Shen, J.H. Perepezko, M.D. Ediger, Increasing the kinetic stability of bulk metallic glasses, Acta Mater. 104 (2016) 25–32, https://doi.org/10.1016/j.actamat.2015.11.048.

[26] J.E.K. Schawe, S. Pogatscher, J.F. Löffler, Thermodynamics of polymorphism in a bulk metallic glass: heat capacity measurements by fast differential scanning calorimetry, Thermochim. Acta 685 (2020) 178518, https://doi.org/10.1016/j.tca.2020.178518.

[27] E. Shoifet, G. Schulz, C. Schick, Temperature modulated differential scanning calorimetry - extension to high and low frequencies, Thermochim. Acta 603 (2015) 227–236, https://doi.org/10.1016/j.tca.2014.10.010.

[28] X. Monnier, D. Cangialosi, B. Ruta, R. Busch, I. Gallino, Vitrification decoupling from α-relaxation in a metallic glass, Sci. Adv. 6 (2020), https://doi.org/10.1126/sciadv.aay1454.

[29] E. Hempel, G. Hempel, A. Hensel, C. Schick, E. Donth, Characteristic length of dynamic glass transition near tg for a wide assortment of glass-forming substances, J. Phys. Chem. B 104 (2000) 2460–2466, https://doi.org/10.1021/jp991153f.

[30] N.G. Perez-de-Eulate, V. Di Lisio, D. Cangialos, Glass transition and molecular dynamics in polystyrene nanospheres by fast scanning calorimetry, ACS. Macro Lett. 6 (2017) 859–863, https://doi.org/10.1021/acsmacrolett.7b00484.

[31] V. Di Lisio, I. Gallino, S.S. Riegler, M. Frey, N. Neuber, G. Kumar, J. Schroers, R. Busch, D. Cangialosi, Size-dependent vitrification in metallic glasses, Nat. Commun. 14 (2023) 4698, https://doi.org/10.1038/s41467-023-40417-4.

[32] K. Schraut, F. Kargl, C. Adam, O. Ivashko, In situ synchrotron XRD measurements during solidification of a melt in the CaO-SiO2system using an aerodynamic levitation system, J. Phys. Condensed Matter 33 (2021), https://doi.org/10.1088/1361-648X/abf7e1.

[33] G. Ashiotis, A. Deschildre, Z. Nawaz, J.P. Wright, D. Karkoulis, F.E. Picca, J. Kieffer, The fast azimuthal integration Python library: pyFAI, J. Appl. Crystallogr. 48 (2015) 510–519, https://doi.org/10.1107/S1600576715004306.

[34] K. Momma, F. Izumi, VESTA 3 for three-dimensional visualization of crystal, volumetric and morphology data, J. Appl. Crystallogr. 44 (2011) 1272–1276, https://doi.org/10.1107/S0021889811038970.

[35] L. Hao, A. Ruban, W. Xiong, CALPHAD modeling based on gibbs energy functions from zero kevin and improved magnetic model: a case study on the Cr–Ni system, CALPHAD. 73 (2021) 102268, https://doi.org/10.1016/j.calphad.2021.102268.

[36] J. Agren, Thermodynamics of supercooled liquids and their glass transition, Phys. Chem. Liquids. 18 (1988) 123–139, https://doi.org/10.1080/00319108808078586.

[37] C.A. Becker, J. John°johnågren, M. Baricco, Q. Chen, S.A. Decterov, U.R. Kattner, J.H. Perepezko, G.R. Pottlacher, M. Selleby, Thermodynamic modelling of liquids: CALPHAD approaches and contributions from statistical physics, Phys. Status Solidi B 251 (2014) 33–52, https://doi.org/10.1002/pssb.201350149.

[38] M. Hillert, B.O. Jansson, B.O. Sundman, J. ~gren, A two-sublattice model for molten solutions with different tendency for ionization, (n.d.).

[39] U.R. Kattner, the Calphad method and its role in material and process development, Tecnol. Metal. Mater. Min. 13 (2016) 3–15, https://doi.org/10.4322/2176-1523.1059.

[40] O. Gross, B. Bochtler, M. Stolpe, S. Hechler, W. Hembree, R. Busch, I. Gallino, The kinetic fragility of Pt-P- and Ni-P-based bulk glass-forming liquids and its thermodynamic and structural signature, Acta Mater. 132 (2017) 118–127, https://doi.org/10.1016/j.actamat.2017.04.030.

[41] N. Neuber, O. Gross, M. Frey, B. Bochtler, A. Kuball, S. Hechler, I. Gallino, R. Busch, On the thermodynamics and its connection to structure in the Pt-Pd-Cu-Ni-P bulk metallic glass forming system, Acta Mater. 220 (2021) 117300, https://doi.org/10.1016/j.actamat.2021.117300.

[42] S.C. Glade, R. Busch, D.S. Lee, W.L. Johnson, R.K. Wunderlich, H.J. Fecht, Thermodynamics of Cu47Ti34Zr11Ni8, Zr52.5Cu17.9Ni14.6Al10Ti5 and Zr57Cu15.4Ni12.6Al10Nb5 bulk metallic glass forming alloys, J. Appl. Phys. 87 (2000) 7242–7248, https://doi.org/10.1063/1.372975.

[43] Z. Evenson, S. Raedersdorf, I. Gallino, R. Busch, Equilibrium viscosity of Zr–Cu–Ni–Al–Nb bulk metallic glasses, Scr. Mater. 63 (2010) 573–576, https://doi.org/10.1016/j.scriptamat.2010.06.008.

[44] S. Inaba, S. Oda, K. Morinaga, Heat capacity of oxide glasses at high temperature region, J. Non. Cryst. Solids. 325 (2003) 258–266, https://doi.org/10.1016/S0022-3093(03)00315-6.

[45] O. Kubaschewski, C.B. Alcock, P.J. Spencer, Materials Thermochemistry, 6th ed., Pergamon Press Oxford, Oxford SE, 1993 r- xii, 363 pages : illustrations ; 26 cmLK-, https://worldcat.org/title/26724109.

[46] M. Frey, R. Busch, W. Possart, I. Gallino, On the thermodynamics, kinetics, and sub-tg relaxations of Mg-based bulk metallic glasses, Acta Mater. 155 (2018) 117–127, https://doi.org/10.1016/j.actamat.2018.05.063.

[47] N. Neuber, O. Gross, M. Eisenbart, A. Heiss, U.E. Klotz, J.P. Best, M.N. Polyakov, J. Michler, R. Busch, I. Gallino, The role of Ga addition on the thermodynamics, kinetics, and tarnishing properties of the Au-Ag-Pd-Cu-Si bulk metallic glass forming system, Acta Mater. 165 (2019) 315–326, https://doi.org/10.1016/j.actamat.2018.11.052.

[48] H.L. Smith, C.N. Saunders, C. Bernal-Choban, S.H. Lohaus, C.J. Stoddard, L. K. Decker, J.Y.Y. Lin, J.L. Niedziela, D.L. Abernathy, J.H. Na, M.D. Demetriou, B. Fultz, Vibrational dynamics in the undercooled liquid of ultra-fragile metallic glasses, Materialia (Oxf) 27 (2023) 101710, https://doi.org/10.1016/J.MTLA.2023.101710.

[49] H.L. Smith, C.W. Li, A. Hoff, G.R. Garrett, D.S. Kim, F.C. Yang, M.S. Lucas, T. Swan-Wood, J.Y.Y. Lin, M.B. Stone, D.L. Abernathy, M.D. Demetriou, B. Fultz, Separating the configurational and vibrational entropy contributions in metallic glasses, Nat. Phys. 13 (2017) 900–905, https://doi.org/10.1038/nphys4142.

[50] Walter. Kauzmann, The nature of the glassy State and the behavior of liquids at low temperatures, Chem. Rev. 43 (1948) 219–256, https://doi.org/10.1021/cr60135a002.

[51] J.E.K. Schawe, J.F. Löffler, Existence of multiple critical cooling rates which generate different types of monolithic metallic glass, Nat. Commun. 10 (2019), https://doi.org/10.1038/s41467-018-07930-3.

[52] S. Mukherjee, Z. Zhou, J. Schroers, W.L. Johnson, W.K. Rhim, Overheating threshold and its effect on time-temperature-transformation diagrams of zirconium based bulk metallic glasses, Appl. Phys. Lett. 84 (2004) 5010–5012, https://doi.org/10.1063/1.1763219.

[53] J.K. Lee, D.H. Bae, W.T. Kim, D.H. Kim, Effect of liquid temperature on thermal stability and crystallization behavior of Ni-based amorphous alloys, Mater. Sci. Eng.: A 375–377 (2004) 332–335, https://doi.org/10.1016/j.msea.2003.10.103.

[54] J. Mao, H.F. Zhang, H.M. Fu, A.M. Wang, H. Li, Z.Q. Hu, The effects of casting temperature on the glass formation of Zr-based metallic glasses, Adv. Eng. Mater. 11 (2009) 986–991, https://doi.org/10.1002/adem.200900174.

[55] Q. Cheng, Y.H. Sun, J. Orava, W.H. Wang, Homogenization of a metallic melt: enhancing the thermal stability of glassy metal, Mater. Today Phys. 31 (2023) 101004, https://doi.org/10.1016/j.mtphys.2023.101004.

[56] Z. Evenson, T. Schmitt, M. Nicola, I. Gallino, R. Busch, High temperature melt viscosity and fragile to strong transition in Zr-Cu-Ni-Al-Nb(Ti) and Cu 47Ti 34Zr 11Ni 8 bulk metallic glasses, Acta Mater. 60 (2012) 4712–4719, https://doi.org/10.1016/j.actamat.2012.05.019.

[57] C. Way, P. Wadhwa, R. Busch, The influence of shear rate and temperature on the viscosity and fragility of the Zr41.2Ti13.8Cu12.5Ni10.0Be22.5 metallic-glass-forming liquid, Acta Mater. 55 (2007) 2977–2983, https://doi.org/10.1016/j.actamat.2006.12.032.

[58] W. Xu, M.T. Sandor, Y. Yu, H.B. Ke, H.P. Zhang, M.Z. Li, W.H. Wang, L. Liu, Y. Wu, Evidence of liquid-liquid transition in glass-forming La50Al35Ni15 melt above liquidus temperature, Nat. Commun. 6 (2015), https://doi.org/10.1038/ncomms8696.

[59] D.H. Kim, W.T. Kim, E.S. Park, N. Mattern, J. Eckert, Phase separation in metallic glasses, Prog. Mater. Sci. 58 (2013) 1103–1172, https://doi.org/10.1016/j.pmatsci.2013.04.002.

[60] P.S. Popel, V.E. Sidorov, Microheterogeneity of liquid metallic solutions and its influence on the structure and properties of rapidly quenched alloys, Mater. Sci. Eng.: A 226–228 (1997) 237–244, https://doi.org/10.1016/s0921-5093(96)10624-9.

[61] X.H. Lin, W.L. Johnson, Formation of Ti-Zr-Cu-Ni bulk metallic glasses, J. Appl. Phys. 78 (1995) 6514–6519, https://doi.org/10.1063/1.360537.

[62] S. Pogatscher, P.J. Uggowitzer, J.F. Löffler, In-situ probing of metallic glass formation and crystallization upon heating and cooling via fast differential scanning calorimetry, Appl. Phys. Lett. 104 (2014) 251908, https://doi.org/10.1063/1.4884940.

[63] N. Neuber, M. Frey, O. Gross, J. Baller, I. Gallino, R. Busch, Ultrafast scanning calorimetry of newly developed Au-Ga bulk metallic glasses, J. Phys. Condensed Matter 32 (2020), https://doi.org/10.1088/1361-648X/ab8252.

[64] S. Mechler, E. Yahel, P.S. Pershan, M. Meron, B. Lin, Crystalline monolayer surface of liquid Au-Cu-Si-Ag-Pd: metallic glass former, Appl. Phys. Lett. 98 (2011) 98–101, https://doi.org/10.1063/1.3599515.

[65] S.V. Ketov, N. Chen, A. Caron, A. Inoue, D.V. Louzguine-Luzgin, Structural features and high quasi-static strain rate sensitivity of Au49Cu26.9Ag5.5Pd2.3Si 16.3 bulk metallic glass, Appl. Phys. Lett. 101 (2012), https://doi.org/10.1063/1.4770072.

[66] M. Frey, N. Neuber, M. Müller, O. Gross, S.S. Riegler, I. Gallino, R. Busch, Determining and modelling a complete time-temperature-transformation diagram for a Pt-based metallic glass former through combination of conventional and fast scanning calorimetry, Scr. Mater. 215 (2022) 114710, https://doi.org/10.1016/j.scriptamat.2022.114710.

[67] A. Kuball, Development, Characterization and Processing of a Novel Family of Bulk Metallic Glasses: Sulfur-containing Bulk Metallic Glasses, Saarland University, 2019, https://doi.org/10.22028/D291-30889.

[68] B.A. Legg, J. Schroers, R. Busch, Thermodynamics, kinetics, and crystallization of Pt57.3Cu14.6Ni5.3P22.8 bulk metallic glass, Acta Mater. 55 (2007) 1109–1116, https://doi.org/10.1016/J.ACTAMAT.2006.09.024.

[69] O. Gross, S.S. Riegler, M. Stolpe, B. Bochtler, A. Kuball, S. Hechler, R. Busch, I. Gallino, On the high glass-forming ability of Pt-Cu-Ni/Co-P-based liquids, Acta Mater. 141 (2017) 109–119, https://doi.org/10.1016/j.actamat.2017.09.013.

[70] J.E.K. Schawe, Measurement of the thermal glass transition of polystyrene in a cooling rate range of more than six decades, Thermochim. Acta 603 (2015) 128–134, https://doi.org/10.1016/j.tca.2014.05.025.

[71] O. Gross, M. Eisenbart, L.Y. Schmitt, N. Neuber, L. Ciftci, U.E. Klotz, R. Busch, I. Gallino, Development of novel 18-karat, premium-white gold bulk metallic glasses with improved tarnishing resistance, Mater. Des. 140 (2018) 495–504, https://doi.org/10.1016/j.matdes.2017.12.007.

[72] R. Busch, The thermophysical properties of bulk metallic glass-forming liquids, JOM 52 (2000) 39–42, https://doi.org/10.1007/s11837-000-0160-7.

[73] G. Wilde, G.P. Görler, R. Willnecker, G. Dietz, Thermodynamic properties of Pd40Ni40P20 in the glassy, liquid, and crystalline states, Appl. Phys. Lett. 65 (1994) 397–399, https://doi.org/10.1063/1.112313.

[74] J.W. CHRISTIAN, in: J.W.B.T.-T.T.of T.in M, A. CHRISTIAN (Eds.), The Theory of Transformations in Metals and Alloys, Pergamon, Oxford, 2002, pp. vi–vii, https://doi.org/10.1016/B978-008044019-4/50001-5.

[75] O. Gross, Precious metal based bulk glass-forming liquids: development, thermodynamics, kinetiks and structure, (2018). doi:10.22028/D291-27993.

[76] E.R. BUCKLE, Reduced temperatures for nucleation in supercooled liquids, Nature 186 (1960) 875–876, https://doi.org/10.1038/186875b0.

[77] R. Busch, E. Bakke, W.L. Johnson, On the glass forming ability of bulk metallic glasses, Mater. Sci. Forum 235–238 (1997) 327–336, https://doi.org/10.4028/www.scientific.net/msf.235-238.327.

[78] C.A. Angell, Formation of glasses from liquids and biopolymers, Science (1979) 267 (1995) 1924–1935, https://doi.org/10.1126/science.267.5206.1924.

[79] R. Böhmer, K.L. Ngai, C.A. Angell, D.J. Plazek, Nonexponential relaxations in strong and fragile glass formers, J. Chem. Phys. 99 (1993) 4201–4209, https://doi.org/10.1063/1.466117.

[80] M. Frey, N. Neuber, O. Gross, B. Zimmer, W. Possart, R. Busch, Determining the fragility of bulk metallic glass forming liquids via modulated DSC, J. Phys. Condensed Matter 32 (2020), https://doi.org/10.1088/1361-648X/ab8526.

[81] I. Gallino, On the fragility of bulk metallic glass forming liquids, Entropy 19 (2017), https://doi.org/10.3390/e19090483.

[82] J. Ding, Y.Q. Cheng, H. Sheng, E. Ma, Short-range structural signature of excess specific heat and fragility of metallic-glass-forming supercooled liquids, Phys. Rev. B Condens. Matter. Mater. Phys. 85 (2012) 1–5, https://doi.org/10.1103/PhysRevB.85.060201.

[83] G. Adam, J.H. Gibbs, On the temperature dependence of cooperative relaxation properties in glass-forming liquids, J. Chem. Phys. 43 (1965) 139–146, https://doi.org/10.1063/1.1696442.

[84] L.-M. Martinez, C.A. Angell, A thermodynamic connection to the fragility of glass-forming liquids, Nature 410 (2001) 663–667, https://doi.org/10.1038/35070517.

[85] L.M. Wang, C.A. Angell, R. Richert, Fragility and thermodynamics in nonpolymeric glass-forming liquids, J. Chem. Phys. 125 (2006), https://doi.org/10.1063/1.2244551.

[86] S. Wei, Z. Evenson, I. Gallino, R. Busch, The impact of fragility on the calorimetric glass transition in bulk metallic glasses, Intermetallics. (Barking) 55 (2014) 138–144, https://doi.org/10.1016/j.intermet.2014.07.018.

[87] B. Bochtler, O. Gross, I. Gallino, R. Busch, Thermo-physical characterization of the Fe67Mo6Ni3.5Cr3.5P12C5.5B2.5 bulk metallic glass forming alloy, Acta Mater. 118 (2016) 129–139, https://doi.org/10.1016/j.actamat.2016.07.031.

[88] D.R. Uhlmann, A kinetic treatment of glass formation, J. Non. Cryst. Solids. 7 (1972) 337–348, https://doi.org/10.1016/0022-3093(72)90269-4.

[89] D.A. Porter, K.E. Easterling, M.Y. Sherif, Phase Transformations in Metals and Alloys, 4th ed., CRC Press, 2021 https://doi.org/10.1201/9781003011804.

[90] Z. Ling, Thermodynamic and Kinetic Study of Pt42.5CuxNi36.5-xP21 Alloy Variations, Saarland University, 2023.

[91] Y.T. Shen, T.H. Kim, A.K. Gangopadhyay, K.F. Kelton, Icosahedral order, frustration, and the glass transition: evidence from time-dependent nucleation and supercooled liquid structure studies, Phys. Rev. Lett. 102 (2009) 6–9, https://doi.org/10.1103/PhysRevLett.102.057801.

[92] Z. Wang, S.V. Ketov, C.L. Chen, Y. Shen, Y. Ikuhara, A.A. Tsarkov, D.V. Louzguine-Luzgin, J.H. Perepezko, Nucleation and thermal stability of an icosahedral nanophase during the early crystallization stage in Zr-Co-Cu-Al metallic glasses, Acta Mater. 132 (2017) 298–306, https://doi.org/10.1016/j.actamat.2017.04.044.

[93] W.L. Johnson, J.H. Na, M.D. Demetriou, Quantifying the origin of metallic glass formation, Nat. Commun. 7 (2016), https://doi.org/10.1038/ncomms10313.